NASA Technical Paper 1086

Metallurgical Characterization of the Fracture of Several High Strength Aluminum Alloys

M. Dilip Bhandarkar and W. Barry Lisagor

DECEMBER 1977

NASA

NASA Technical Paper 1086

Metallurgical Characterization of the Fracture of Several High Strength Aluminum Alloys

M. Dilip Bhandarkar and W. Barry Lisagor
Langley Research Center
Hampton, Virginia

NASA
National Aeronautics
and Space Administration

**Scientific and Technical
Information Office**

1977

SUMMARY

A large volume of information on the fracture behavior of aluminum alloys has been generated under test conditions which have not been controlled in a systematic fashion. As a result, metallurgical characterization of fracture behavior is incomplete and scattered in the literature.

The main objective of this investigation was to study systematically, under controlled monotonic loading conditions, the fracture behavior of common structural aluminum alloys in relation to their microstructures. Thin sheets and thick plates of commercial aluminum alloys 2024, 6061, 7075, and 7178 (in selected heat treatments) were tested at room temperature in shear, tensile, and notch-bend tests. Fracture surface morphologies were examined for different strain rates and for both longitudinal and transverse orientations. The several different types of second-phase particles observed on fracture surfaces and metallographic sections were chemically analyzed using scanning electron microscopy and associated energy dispersive X-ray analysis (designated edax).

Several different types of second-phase particles, some not reported by other investigators, were identified in the alloys. The results indicated that grain structure, size and distribution of precipitates, type of test load, and the form of commercial product considerably affected fracture morphology. Specimen orientations examined in the present investigation had little influence on fracture morphology. Strain rate changes of two to three orders of magnitude did not alter the strength properties and fracture behavior of tensile specimens. One to two orders of magnitude change in shear strain rate considerably affected the shear strength of all the alloys examined, and shear fracture morphology was altered in all alloys except 6061. This unusual behavior was explained on the basis of the differences in second-phase particle cracking.

In analyzing failures that occur under complex service conditions, characteristic features of the type described in this paper should prove useful for establishing the fracture mechanisms and other factors contributing to the cause of failure.

INTRODUCTION

Fractographic analysis of microscopic fracture processes has assumed increasing importance in studies of material failures occurring in service. A complete understanding of the microscopic in-service fracture processes that occur under complex conditions of loading and chemical environments requires characterization of the morphology of fracture surfaces produced under several controlled loading conditions. Attempts have been made to relate microstructure of materials to their fracture behavior. Several such investigations have been conducted on aluminum alloys. Some investigators have identified certain fracture mechanisms in these alloys and have discussed the influence of microstruc-

tural variables such as grain structure and precipitate distribution on fracture morphology. (See refs. 1 to 11.) However, most reported investigations have not been systematic in their approach to alloys and heat treatments, types of commercial products, test specimen geometries, and testing conditions. As a result, only scattered information exists in the literature on fracture of aluminum alloys.

The main objective of the present investigation was to characterize the fracture morphology of commercial aluminum alloys 2024, 6061, 7075, and 7178 (in selected heat treatments) as a function of several controlled loading conditions. Attempts were made to relate fracture behavior to microstructure, form of commercial product, test specimen geometry and orientation, and testing conditions. The documented results for these aluminum alloys should aid in analyzing in-service material failures.

The units for the physical quantities defined in this paper are given in the International System of Units (SI) and parenthetically in U.S. Customary Units. Measurements and calculations were made in U.S. Customary Units. Factors relating the two systems are given in reference 12.

EXPERIMENTAL PROCEDURE

Materials

The investigation included aluminum alloys 2024, 6061, 7075, and 7178 in sheet and plate forms which are commonly employed in structural application in the aerospace industry. Sheets were 1 mm (0.040 in.) thick and plates were 25.4 mm (1 in.) thick. Chemical compositions of the alloys are listed in table I. Heat treatments and materials specifications of the alloys are listed in table II.

Specimens and Mechanical Tests

Tensile tests were conducted using thin sheet specimens 12.7 mm (0.5 in.) wide in the gage section and round specimens 12.7 mm (0.5 in.) in diameter in the gage section. The round specimens were machined from thick plates of the alloys. Both the tensile sheet and the plate specimens were tested in accordance with the standard American Society of Testing Materials (ASTM) tension testing procedure (E8-69) under three strain rate conditions until fracture: (1) 0.005/min; (2) 1.5/min; and (3) 0.005/min to yield followed by 0.05/min. Shear tests were performed using thin sheet specimens in accordance with the procedure detailed in appendix A. The specimens were tested at cross-head displacement rates of 2.54 mm/min (0.1 in./min) and 76.2 mm/min (3 in./min). Tensile and shear properties were determined for both longitudinal and long transverse specimens. Three point bend tests were performed on single-edge-notched fatigue-precracked specimens with a nominal thickness of 12.7 mm (0.5 in.) and a nominal width of 25.4 mm (1.0 in.). The specimens were machined from thick plates of the alloys with the crack plane perpendicular to both the longitudinal and transverse directions and the crack front propagating in the short-transverse direction. Maximum stress intensity factors (K_{IQ}) at failure were obtained from

the test data. Additional test details of notch-bend tests and the specimen sketch can be found in appendix B.

Metallurgical and Fractographic Analysis

Metallographic specimens were prepared using standard hand polishing techniques. Specimens were successively ground on 180-, 240-, 320-, and 600-grit wet silicon carbide paper and successively polished using 6 μm (2×10^{-4} in.) diamond, 0.3 μm (0.1×10^{-4} in.) alumina, and 0.05 μm (0.02×10^{-4} in.) alumina. Etch-polish-etch procedures were used employing Keller's reagent (2.5 percent HNO_3, 1.5 percent HCl, 0.5 percent HF, balance H_2O).

Microstructure and fracture surface morphology were characterized using the optical microscope and the scanning electron microscope. Second-phase particles that were observed on fracture surfaces and metallographically polished sections of the alloys were analyzed using the scanning electron microscope and associated energy dispersive X-ray chemical analysis (edax). The particle analysis procedure is detailed in appendix C.

RESULTS

Mechanical property data resulting from the various tests conducted to produce the fracture surfaces are presented in tables III to VI. Tables III and IV contain mechanical property and tensile property results, respectively, for plate and sheet tests. Tables V and VI contain test results on the effect of strain rate on tensile and shear specimens, respectively. These data are discussed more fully in sections where they are used to support fracture morphology descriptions. Table VII provides an index relating microstructure, particle analysis, and fracture morphology with the numbers of the figures which characterize them. Laboratory analysis included extensive microscopy of all types of fractures produced. Many photomicrographs which were obtained were not used in the report. The photomicrographs contained in the report were selected because they best illustrate the technical results presented.

Microstructures of Alloys

Both optical microscopy and scanning electron microscopy were used for microstructural examination of alloys of the present investigation. The grain structures and second-phase particle distributions were better revealed in optical micrographs. Therefore, except in one case, only optical micrographs are presented to illustrate these microstructural features. The more important use of scanning electron microscopy in microstructural examination was in the edax chemical analysis of second-phase particles on polished and fractured surfaces. The results of microstructural examination are presented in this paper.

Plate Specimens

Aluminum alloy 2024-T351.- Typical micrographs and edax patterns are shown in figure 1 for a plate specimen of 2024-T351. The edax patterns show X-ray intensity peaks of the characteristic radiation of each element present. The elements are labeled with their chemical symbol above or beside the respective element signal. The edax patterns display the characteristic energy level (kev) associated with each element on the abscissa and the intensity level (related to amount of element present) on the ordinate of each plot. The optical micrograph of figure 1(a) clearly shows the elongated grains and a high density of large second-phase particles. A large fraction of the particles visible in figure 1(a) were in two size ranges, 0.4 to 1 μm (1.5×10^{-5} to 4×10^{-5} in.) and 3 to 10 μm (1×10^{-4} to 4×10^{-4} in.). Also faintly visible, but not resolved, in figure 1(a) is a dispersion of a finer precipitate which formed during the aging treatment. The scanning electron micrographs of figures 1(b) and 1(c) illustrate some of the coarse particles that were commonly observed in the alloy. A few coarse particles in the alloy were as large as 14 μm (6×10^{-4} in.). The coarse particles in the alloy were primarily of three types:

(a) Particles labeled A in figures 1(b) and 1(c) exhibited X-ray intensity peaks of Al and Cu in the edax pattern, as shown in figure 1(d). The intensity ratio for Cu and Al suggested that the particles were $CuAl_2$. A Mg peak was detected for some particles suggesting the presence of $CuMgAl_2$. The compounds $CuAl_2$ and $CuMgAl_2$ are the hardening phases that precipitate during aging, but not in the large sizes shown in figure 1. Other investigators have reported that large particles of these two types result from ineffective solution treatment (refs. 13 and 14).

(b) Particles labeled B in figures 1(b) and 1(c) exhibited X-ray intensity peaks of Al, Fe, Mn, Cu, and Si as shown in the edax pattern in figure 1(e). The literature contains no evidence of the presence of particles of this chemical composition in aluminum alloy 2024. However, Featherby (ref. 15) has reported particles containing the same elements in aluminum alloy 2219.

(c) A small number of particles observed in the alloy were characterized by X-ray intensity peaks of Al, Cu, Fe, and Mn. These are labeled C in figure 1(c). The edax pattern is shown in figure 1(f). The X-ray intensity ratios suggest that these particles are (Cu, Fe, Mn) Al_6. Particles of this type have been reported in aluminum alloy 2024 by other investigators (ref. 14).

The fracture surfaces of plate tensile and precracked notch-bend specimens of the alloy contained the three types of particles just described.

Aluminum alloys 6061-T4 and 6061-T651.- Optical micrographs of plate specimens of aluminum alloys 6061-T4 and 6061-T651 are shown in figure 2. The two microstructures were very similar and were characterized by coarse particles of sizes 1 to 10 μm (0.4×10^{-4} to 4×10^{-4} in.) and a dense, uniform distribution of finer particles. The dispersion of the strengthening precipitate was expected to be different in the alloys since the aging treatments were different. Grain boundaries were rarely revealed in the alloys. Considerable banding of precipitates was common to both alloys as is evident in the figure. Chemical analysis revealed three types of coarse second-phase particles in the alloys:

(a) Particles exhibiting X-ray intensity peaks of Al, Fe, Si, Cr, and Mn were very common in the alloys. The edax pattern in figure 2(c) illustrates the chemical analysis. Particles of this type have not been reported in the literature.

(b) A few well-rounded particles 5 to 7 μm (2×10^{-4} to 3×10^{-4} in.) in size which exhibited Al, Mg, and Si X-ray peaks were also observed in the alloys. Intensity ratios in edax patterns suggested that the particles were Mg_2Si. A typical edax pattern is illustrated in figure 2(d). The Al peak in the pattern resulted from matrix contribution. The compound Mg_2Si is the primary hardening precipitate forming during aging in alloy 6061, but large particles of this phase are often present in the alloy because of ineffective homogenization (refs. 13 and 14).

(c) A few Si particles were also observed in the alloys. The types of particles just described were observed in large dimples on fracture surfaces of tensile bars and precracked notch-bend specimens.

Aluminum alloy 7075-T651.- The microstructure of plate specimens of aluminum alloy 7075-T651 was characterized by an elongated grain structure and heavy banding. The bands and grain boundaries had a high density of second-phase particles. Coarse constituent particles and finer strengthening dispersoid particles were very common, as illustrated by the optical micrographs of figure 3. The grain dimension in the direction of plate thicknesses was 10 to 20 μm (4×10^{-4} to 8×10^{-4} in.). Chemical analysis of second-phase particles revealed several different types of particles in the alloy plate specimens. These are described as follows:

(a) Particles exhibiting X-ray intensity peaks of Fe, Al, Cu, Cr, Mn, Zn, and Mg were oblong shaped and were very common in the alloy. A typical edax pattern is illustrated in figure 4(a) for this type of particle. Comparison of the pattern with matrix analysis indicated that the Mg intensity resulted from matrix contribution. The literature contains no evidence of the presence of this type of particle in aluminum alloy 7075-T6. In the present investigation, these particles were very commonly observed as cleaved-on fracture surfaces of precracked notch-bend specimens, but were rare on fracture surfaces of plate tensile specimens.

(b) Particles exhibiting X-ray intensity peaks of Al, Cu, Fe, Zn, Cr, Mn, and Mg were very common in the alloy. An edax pattern for the particles is shown in figure 4(b). Comparison with matrix chemical analysis indicated that the Mg intensity peak in figure 4(b) was caused by matrix contribution. The particles were somewhat similar to those described in section (a), but exhibited a Cu peak that was stronger than the Fe peak. This type of particle was usually found fragmented on the fracture surfaces of tensile and notch-bend specimens. Particles of this type have not been reported in the literature.

(c) Particles exhibiting X-ray intensity peaks of Al, Fe, Cr, Si, Mn, and Cu were sometimes observed in dimples on fracture surfaces of notch-bend specimens. They were not observed on fracture surfaces of plate tensile specimens. An edax pattern is shown in figure 4(c) for the particles. Comparison with a matrix pattern showed that parts of the Al and Cu peaks in figure 4(c) were

caused by matrix contribution. Particles of this type have not been reported in the literature.

(d) Particles 4 to 6 μm (1.6×10^{-4} to 2.4×10^{-4} in.) in size exhibiting X-ray intensity peaks of Mg, Si, and Al were observed frequently on fracture surfaces of notch-bend specimens, but no on fracture surfaces of plate tensile specimens. A typical edax pattern for this type of particle is shown in figure 4(d). The aluminum peak intensity in the pattern resulted from matrix contribution (see appendix C). The Mg to Si intensity ratio suggested that the particles were Mg_2Si. Low et al. (ref. 6) have reported similar particles in aluminum alloy 7075.

(e) Several particles on fracture surfaces of precracked notch-bend specimens showed X-ray intensity peaks of Mg, Al, Si, Cu, and Zn. Some of these particles were rich in Cu and Mg with a Cu to Mg peak ratio of approximately 2. A comparison with matrix analysis suggested that the Al and Zn peaks resulted, in part, from matrix contribution. An edax pattern is shown in figure 4(e) for the particles. The relative intensities of peaks suggest that these particles are $CuMgAl_2$ with a small amount of Si in solid solution. On fracture surfaces of notch-bend specimens, these particles were cleaved but not fragmented. They were not observed on fracture surfaces of plate tensile specimens.

(f) Another type of particle often observed on fracture surfaces of notch-bend specimens of aluminum alloy 7075-T651 exhibited the same intensity peaks as particles in section (e). The edax pattern for the particles is shown in figure 4(f). A comparison of figures 4(e) and 4(f) indicates that in figure 4(f) the Mg and Si peaks are more prominent with an intensity ratio of approximately 2. Particles with the chemical composition illustrated by figure 4(f) were fragmented, not simply cleaved, on fracture surfaces of notch-bend specimens. They were not observed on fracture surfaces of plate tensile specimens. Complex particles of this composition have not been reported elsewhere.

Aluminum alloy 7178-T651.- Optical micrographs illustrating the microstructure of a plate specimen of aluminum alloy 7178-T651 are shown in figure 5. Elongated grain structures and high density of second-phase particles at grain boundaries are evident in the figure. Coarse particles 3 to 8 μm (1×10^{-4} to 3×10^{-4} in.) in size and fine particles smaller than 1 μm (0.4×10^{-4} in.) were present in the alloy. A few coarse particles were as large as 15 μm (6×10^{-4} in.). Chemical analysis by edax showed that the coarse second-phase particles were of three types:

(a) Particles exhibiting X-ray intensity peaks of Al, Fe, Zn, Cu, Cr, Mn, and Mg were commonly observed as cleaved particles in dimples on the fracture surfaces of plate tensile and precracked notch-bend specimens. The edax pattern obtained for these particles is shown in figure 6(a). The Mg intensity and parts of the Al and Zn intensities in figure 6(a) resulted from matrix contribution. No particles of this type have been reported in the published literature.

(b) Another type of commonly observed particle was characterized by X-ray intensity peaks of Al, Cu, Mg, Si, and Zn, as illustrated in figure 6(b). The Mg and Zn intensity peaks resulted from matrix contribution. Particles of this type were cleaved during the fracture process and were left in the dimples

observed on fracture surfaces of both the plate tensile specimens and the notch-bend specimens. The Si intensity peak was weak and the relative peak intensities suggest that the particles were $CuAl_2$, containing Si in solid solution.

(c) Particles exhibiting X-ray intensity peaks of Al, Cu, Mg, and Zn were occasionally observed in the alloy. An edax pattern for the particles is shown in figure 6(c). The difference between these particles and those in section (b) was that the Mg intensity peak was considerably stronger and was not entirely from matrix contribution. Also the Si intensity peak was absent. The X-ray intensity ratios suggested that the particles were $CuMgAl_2$.

Sheet Specimens

Optical micrographs of longitudinal sections of the alloys are illustrated in figure 7. The general features in the microstructures were the same as those observed from plate specimens. The main difference was that the microstructures of sheet specimens exhibited less banding than did microstructures of plate specimens.

The fracture surfaces of sheet tensile specimens of aluminum alloy 2024-T3 contained the same three types of second-phase particles as were found in the plate specimens of the alloy 2024-T351 (analyzed in fig. 1). The sheet shear specimens of 2024-T3 contained only two types of particles having chemical compositions similar to those analyzed in figures 1(d) and 1(e) for 2024-T351 plate specimens.

The fracture surfaces of aluminum alloys 6061-T4 and 6061-T6 sheet tensile and shear specimens contained predominantly one type of second-phase particle. The edax pattern was similar to the one obtained for the type of particles in the plate specimens of 6061-T4 analyzed in figure 2(c). The only difference was the absence of a weak Si peak for particles in the sheet specimens.

The fracture surfaces of sheet tensile specimens of aluminum alloy 7075-T6 contained three types of second-phase particles. The edax analysis for one type is shown in figure 8(a) where intensity peaks of Al, Fe, Cu, and Zn are seen. A comparison with matrix analysis showed that the Cu, Zn, and a portion of the Al intensity resulted from matrix contribution. The X-ray intensity data suggested that these particles were $FeAl_3$. The second type of particles observed on fracture surfaces of sheet tensile specimens of 7075-T6 were similar to those analyzed in figure 4(e) for the plate specimen of 7075-T651. The third type of particles exhibited Al, Cu, and Zn peaks as shown in the edax pattern of figure 8(b). These particles are probably Cu_3ZnAl_3 which has been reported to form in aluminum alloys (ref. 16). The sheet shear specimens of the alloy exhibited a predominance of particles identical to those analyzed in figure 8(a) for sheet tensile specimens. A small number of particles in shear specimens had the same chemical analysis as that shown in figure 4(c) for particles in plate specimens of 7075-T651.

The sheet tensile specimens of aluminum alloy 7178-T6 exhibited two types of particles on their fracture surfaces. One type was similar to the particles found in 7075-T6 sheet and had the chemical analysis illustrated in figure 8(a).

These particles were more commonly observed than the second type that yielded X-ray peaks of Al, Cu, Zn, and Mg as illustrated in figure 9. The sheet shear specimens of the alloy contained only one type of second-phase particle on their fracture surfaces. These particles yielded edax patterns illustrated in figure 10. The predominant peaks were Al, Cu, Fe, and Zn. Weak Cr and Mn peaks were also found. The chemical compositions of particles observed on sheet fracture surfaces of 7178-T6 were different from the compositions of particles observed in 7178-T651 plate specimens. This difference is evident from a comparison of the edax patterns in figures 6, 9, and 10. The edax pattern shown in figure 10 for particles observed on shear fracture surfaces of 7178-T6 revealed the presence of the same elements that were present in the type of particles in thick plates of the alloy characterized by the edax pattern in figure 6(a). However, the relative intensities of the peaks of the elements were different in the two cases.

Characterization of the Fracture Morphology of Alloys

Plate tensile specimens.- Typical scanning electron fractographs are shown in figure 11 for plate tensile specimens of alloys examined in the present investigation. The specimens were tested at a strain rate of 0.005/min and the resulting mechanical property data are listed in table III. Strain rate effects on ultimate tensile strength are shown in table V. The predominant failure mode observed in the plate specimens of aluminum alloys 2024-T351, 6061-T4, and 6061-T651 was microvoid coalescence, typically characterized by equiaxed dimple appearance. In contrast, the fracture surfaces of alloys 7075-T651 and 7178-T651 exhibited a predominance of regularly formed facets that appeared relatively smooth at low magnifications.

There were differences, however, in the sizes and shapes of dimples observed in the alloys. Some unique features of the dimpled rupture in alloy 2024-T351 are illustrated by the scanning electron fractographs in figure 12. The nonuniform dimple sizes and the irregular dimple shapes are evident in both fractographs. The larger dimples on fracture surfaces of the alloy contained large second-phase particles (2 to 10 μm (0.8×10^{-4} to 4×10^{-4} in.) in diameter) that were shattered into several fragments. However, a few particles as large as 14 μm (6×10^{-4} in.) in diameter were also observed. Areas between large dimples often appeared smooth at low magnification (fig. 11(a)), but examination at progressively higher magnifications revealed microscopic roughness and extremely fine dimples. Roughness and fine dimples are readily visible in areas labeled A in figure 12(a). The fine dimples visible in figure 12(b) are generally smaller than about 0.5 μm (0.2×10^{-4} in.) in diameter, and were probably nucleated at the fine strengthening precipitates that form in the alloy during the aging treatment. Both the longitudinal and the transverse specimens of the alloy exhibited the same types of fracture features, but extensive examination of the fracture surfaces of the two specimens indicated that in the transverse specimen, smooth areas with fine dimples were less predominant, and the fracture morphology was primarily characterized by large dimples.

Dimples were more distinct and more regularly shaped on the fracture surfaces of aluminum alloy 6061-T4 than on those of aluminum alloy 2024-T351. As illustrated by the scanning electron fractographs in figures 11(b) and 13, frac-

ture morphology in the 6061-T4 specimen was characterized by clusters of large dimples. The dimple clusters were separated by areas which appeared relatively smooth at low magnifications as shown in figure 13(a). Examination of these areas at high magnifications revealed fine dimples (less than 1 μm (0.4×10^{-4} in.) in diameter) similar to those in the plate tensile specimens of aluminum alloy 2024-T351. The dimples are illustrated at A in figure 13(b). Both the longitudinal and the transverse specimens exhibited similar fractures.

As illustrated by the scanning electron fractographs in figures 11(c) and 14, large equiaxed dimples in aluminum alloy 6061-T651 were better defined and more regularly shaped than in alloys 2024-T351 and 6061-T4. The larger dimples contained cleaved second-phase particles 5 to 10 μm (2 to 4×10^{-4} in.) in size and were separated in many instances by thin ligaments containing fine dimples with diameters smaller than 1 μm (0.4×10^{-4} in.). Both the longitudinal and the transverse specimens exhibited a similar fracture morphology.

As stated earlier, microvoid coalescence, leading to the formation of dimples, was the predominant failure mode in plate tensile specimens of aluminum alloys 2024-T351, 6061-T4, and 6061-T651. However, in plate tensile specimens of alloys 7075-T651 and 7178-T651, the predominant portion of the fracture was characterized by relatively smooth and flat facets. The scanning electron fractographs in figures 11(d), 11(e), 15, and 16 illustrate these features. In both alloys, the areas between the smooth facets exhibited fracture features indicative of ductile tearing and dimple formation. The dimples were not distinct and appeared as pockets containing cracked second-phase particles, as illustrated at A in figure 15(b). Regions of ductile tearing are indicated at B in the figure. The smooth facets observed in 7075-T651 and 7178-T651 were approximately parallel to the plane of maximum shear stress in the tensile specimens (approximately parallel to the plane at 45° to the applied load). This orientation and their smooth appearance suggested that the facets were stretched regions formed by extensive shearing and tearing along glide planes. The facets revealed fine, shallow, and poorly defined dimples which possibly resulted from material failure around the precipitate particles that constitute the strengthening dispersion in the alloy. The fine dimples in the 7178-T651 specimen are illustrated by the scanning electron fractograph in figure 17, a more highly magnified view of an area near the center of figure 11(e). In both 7075-T651 and 7178-T651, fracture morphology was the same for longitudinal and transverse specimens.

Tensile sheet specimens.- Microvoid coalescence, leading to dimpled rupture, was the primary mode of failure in the thin sheet specimens of all the alloys of the present investigation, as is evident from the scanning electron fractographs in figure 18. The specimens were tested at a strain rate of 0.005/min. Tensile properties are listed in table IV, and effects of strain rate on ultimate tensile strength are shown in table V. Typically, the dimples were of two types, equiaxed and elongated. Large and small equiaxed dimples were observed in local fracture areas that were approximately normal to the applied load. Large and small elongated dimples occurred in local fracture areas inclined to the load, resulting from failure produced by a shear stress component in addition to the normal stress component. The large dimples (both equiaxed and elongated) appeared to be nucleated primarily by fracture of second-phase particles and were generally 5 to 8 μm (2×10^{-4} to 3×10^{-4} in.) in

diameter. The fine dimples were less than 1 μm (0.4×10^{-4} in.) in diameter and were nucleated possibly by dispersoid strengthening particles. Although the fractures of sheet specimens of all alloys of the present investigation exhibited the features described earlier, the alloys differed both in the macroscopic and the microscopic fracture morphologies as follows.

Microscopically, the large dimples in both the longitudinal and the transverse specimens of aluminum alloy 2024-T3 were generally separated by thin ligaments containing fine dimples, as illustrated in figure 19. Many local regions of failure in sheet tensile specimens of the alloy were similar to those observed in the shear test specimens of the alloy (discussed in a later section). As illustrated in figure 20 for a longitudinal sheet tensile specimen, these local regions of shear failure exhibited an abundance of relatively smooth areas which contained dimples of submicron size. Such areas were not uniformly distributed throughout the entire fracture surface but occurred in varying proportions in different parts of the specimen fracture surface. Extensive scanning electron microscopy of the fracture surfaces of the longitudinal and transverse specimens showed that smooth areas were more dominant for the transverse specimens than for the longitudinal specimens.

Both the 6061-T4 and the 6061-T6 aluminum alloys exhibited shear lips extending from the specimen surfaces up to a considerable portion of the specimen thickness, as illustrated in figures 21(a) and 21(b), respectively. The large dimples in both alloys were very uniform as is evident from figures 22(a) and 22(b) for 6061-T4 and 6061-T6, respectively. The average spacing of the dimples in 6061-T6 was greater than the spacing of dimples in 6061-T4.

Sheet tensile specimens of aluminum alloys 7075-T6 and 7178-T6 failed predominantly by dimpled rupture under a normal stress, and shear failure was less prevalent than in other alloys. The dimples that formed under a normal stress in these two alloys appeared somewhat different from the dimples formed under a normal stress in other alloys. Scanning electron fractographs shown in figures 23(a) and 23(b) illustrate the dimpled rupture in 7075-T6 and 7178-T6, respectively. A comparison of figures 22 and 23 shows that dimples were less uniform in 7075-T6 and 7178-T6 than in 6061-T4 and 6061-T6. In addition, the fracture surfaces of 7075-T6 and 7178-T6 exhibited grooves and secondary cracks (labeled A in fig. 23) bounded by walls that appeared relatively smooth.

Shear specimens.- Thin sheet specimens, tested in shear, of all alloys of the present investigation were much alike in fracture appearance. Macroscopically, the fracture surfaces were planar and smooth with no irregularities. Ultimate shear strengths are listed in table VI.

Typical scanning electron fractographs are shown in figure 24 for the alloys. The specimens were tested under a cross-head separation rate of 2.54 mm/min (0.1 in./min). In all alloys, the longitudinal and transverse specimens exhibited similar fractures. Microscopically, the fractures were characterized by shallow shear dimples which were elongated in the shear direction. Several areas appeared rather smooth at low magnifications (about X200), but when examined at higher magnifications, these ar revealed dimples of submicron size. The fine dimples are illustrated in figure 25 for a 2024-T3 shear specimen. The fractograph was obtained by magnifying the area near A of

the fractograph shown in figure 24(a). The width of dimples on the shear fracture surfaces of the alloys varied from less than 1 to 10 μm (0.4×10^{-4} to 4×10^{-4} in.).

In spite of the similarities of fractures shown in figure 24, some minor differences were noted among the fractures of different aluminum alloys. The aluminum alloy 2024-T3 exhibited large second-phase particles on the fracture surface. These particles were cracked and were evidently the sites of nucleation of large dimples. Particle sizes varied from 1 to 10 μm (0.4×10^{-4} to 4×10^{-4} in.). Cracked particles were also observed in the large shear dimples of other alloys, but were less frequently observed than in 2024-T3; a major part of the fracture propagated through the matrix without disturbing the large particles. The fracture mode resulted in formation of fine shear dimples, apparently nucleated by strengthening precipitates.

In some areas near the center of the transverse specimen of aluminum alloy 7178-T6, stringer-like features were observed, as illustrated in figure 26(a). A cellular type of dimple structure was evident in the stringers as shown in figure 26(b).

Fatigue-precracked notch-bend specimens.- Microvoid coalescence, leading to dimpled rupture, was a predominant failure mode in the thick fatigue-precracked notch-bend specimens of aluminum alloys 2024-T351, 6061-T4, and 6061-T651 (figs. 27 to 30). The sizes and shapes of dimples were different in different alloys. The fracture of 7075-T651 (figs. 31 and 32) primarily occurred by the formation of relatively smooth facets. The facets were separated by tear ridges, pockets containing cracked particles, and secondary cracks. The 7178-T651 specimens (fig. 33) exhibited dimpled rupture as well as features that were characteristic of the 7075-T651 specimen. Maximum stress intensity values are listed in table III. The fracture morphologies are further discussed in detail later in this section for each of the alloys. The discussion is limited to the general appearance of the static portion of the fracture surfaces.

In the aluminum alloy 2024-T351, dimpled rupture occurred by the formation of dimple colonies separated by relatively smooth areas as shown in figure 27(a). Dimples were typically of two sizes, large dimples 6 to 20 μm (2×10^{-4} to 8×10^{-4} in.) in diameter and fine dimples less than 1 μm (0.4×10^{-4} in.) in diameter. Large cracked second-phase particles were observed in the large dimples. Particle sizes ranged from 3 to 10 μm (1×10^{-4} to 4×10^{-4} in.). These features are illustrated by the scanning electron fractographs of figures 27(b) and 27(c). Both the longtudinal and the transverse specimens exhibited similar fractures. As illustrated in figure 28, the fracture surfaces of both specimens were relatively planar on a macroscopic scale and there were no shear lips.

Precracked notch-bend specimens of aluminum alloys 6061-T4 and 6061-T651 were similar to each other in fracture morphology. Macroscopically, both fractures exhibited extensive shear lips as illustrated in figure 29. On a microscopic scale, the fracture surfaces of both alloys were characterized by dimpled rupture which was somewhat similar to that in 2024-T351. However, the dimples in 6061-T4 and 6061-T651 were equiaxed and well formed unlike the more irregular dimples in the 2024-T351 specimens. In the 6061-T651 alloy specimen,

clusters of large (greater than 10 μm (4×10^{-4} in.) in diameter) equiaxed dimples were separated by areas with small dimples and other areas which appeared smooth when examined at low magnifications. These features are illustrated by the scanning electron fractograph of figure 30(a). On examination at high magnification, shallow dimples 1 to 2 μm (0.4×10^{-4} to 0.8×10^{-4} in.) in diameter were revealed in the smooth areas. An extremely fine cellular structure was evident in the shallow dimples. The fine dimples and the cellular structure are illustrated in figures 30(b) and 30(c). The large dimples contained cracked second-phase particles 5 to 7 μm (2×10^{-4} to 3×10^{-4} in.) in diameter and fragmented particles with diameters as large as 20 μm (8×10^{-4} in.).

Precracked notch-bend specimens of aluminum alloy 7075-T651 exhibited some ductile tearing and dimpled rupture, but microvoid coalescence was not the predominant failure mode. Instead, the fracture was characterized primarily by relatively smooth and flat facets. Figure 31(a) shows that although the facets for a transverse specimen were of the same type as those observed in the plate tensile specimens of the alloy, they were more regularly formed than those in the plate specimens. The regular formation was possibly due to the controlled crack propagation that was initiated at the fatigue crack tip. The widths of the facets were 10 to 50 μm (4×10^{-4} to 20×10^{-4} in.). The facets were separated by tear ridges and large dimple-like pockets containing cracked second-phase particles 4 to 12 μm (2×10^{-4} to 5×10^{-4} in.) in size. Frequently, the particles observed were fragmented. At high magnifications, fine submicron size dimples were revealed on the smooth facets, as illustrated by the scanning electron fractograph in figure 31(b). This fractograph is a high magnification image of a facet near the center of the fractograph shown in figure 31(a). The small dimples were possibly nucleated at precipitate particles that constitute the strengthening dispersion in the alloy.

Secondary cracks approximately normal to the fracture plane, and deep grooves were also commonly observed in precracked notch-bend specimens of aluminum alloy 7075-T651. These features are illustrated by the scanning electron fractographs in figure 32. The nature and possible causes of these features are discussed in a later section.

The precracked notch-bend fracture of aluminum alloy 7178-T651 was similar in many respects to the fracture of 2024-T351 notch-bend specimens. As illustrated by the low magnification fractograph of figure 33(a), the fracture was characterized by a fairly regular array of dimpled and relatively smooth areas. At higher magnifications, roughness and dimples of submicron size were revealed in the smooth areas as shown in figures 33(b) and 33(c). Higher magnification fractographs of dimpled areas (figs. 33(d) and 33(e)) revealed large dimples (3 to 8 μm (1×10^{-4} to 3×10^{-4} in.) in diameter) containing second-phase particles (at A), fine dimples (about 0.2 μm (0.08×10^{-4} in.) in diameter) in areas between large dimples (at B), and areas indicating ductile tearing (at C). Deep grooves and secondary cracks of the type observed in precracked notch-bend specimens of 7075-T651 were also observed in aluminum alloy 7178-T651.

Macroscopically, precracked notch-bend specimens of both 7075-T651 and 7178-T651 fractured in a relatively planar mode with very thin shear lips. This was also true for the 2024-T351 notch-bend specimens.

DISCUSSION

Microstructural Effects on Fracture

Several investigators have examined the role of precipitates and inclusions in the fracture process (refs. 4, 6, 8, 11, and 15); they generally agree that such particles can participate in the fracturing process by acting as nucleating sites for microcracks and voids. Large and brittle particles crack easily at low plastic strains while small particles crack less readily. Particles with weak bonding to the matrix induce failure by nucleating microvoids at the particle-matrix interfaces. Under continued deformation, microcracks and microvoids grow to form larger voids. The final stage of fracture usually involves either the coalescence of voids by continued growth or the joining of voids already formed by the tearing of the ligaments between them. Microvoid coalescence results in a dimpled fracture morphology. The size, shape, and spacing of dimples are influenced by the nature, size, and distribution of the second-phase particles in the alloys. In commercial aluminum alloys, several different intermetallic compounds can participate in the fracture process. As discussed in an earlier section, several types of second-phase particles were identified in the alloys examined in the present investigation. In the discussion that follows, an attempt is made to relate the fracture morphology of the alloys to their microstructure.

In the plate tensile and precracked notch-bend specimens of aluminum alloy 2024-T351, precipitate particles of a wide range of sizes appeared to be involved in the fracture process. The larger (>2 μm (>1 × 10^{-4} in.)) particles nucleated voids by cracking. The growth of such voids resulted in the formation of the large dimples that were observed on the fracture surfaces of these specimens. Fine dimples observed in ligaments between large dimples were nucleated probably by failure at or near particle-matrix interfaces of finer particles. Both large dimples and finer dimples are illustrated in figures 11(a) and 12. In thin sheet tensile specimens of aluminum alloy 2024-T3, particles larger than 8 μm (3 × 10^{-4} in.) were rarely observed on fracture surfaces. (See figs. 18(a) and 19.) Finer particles appeared to nucleate microvoids more readily in thin sheets of the alloy than in thick plates. A possible reason for this behavior is the plane stress condition in thin sheets which promotes plastic deformation and void nucleation, and thus lead to the formation of a large number of fine dimples. This was also evident in the shear fractures of thin sheets of aluminum alloy 2024-T3, illustrated in figure 24(a), where the shearing process involved the formation of dimples at particles of a wide range of sizes; but a large portion of the fracture propagation occurred through the matrix containing fine particles and led to the formation of fine dimples.

Tensile and notch-bend fractures of aluminum alloys 6061-T4 and 6061-T651 exhibited dimples that were more distinct and regularly formed than the dimples in other alloys examined in the present investigation. (See, for example, fig. 11.) The sizes, shapes, distributions, and volume fractions of large (>2 μm (>1 × 10^{-4} in.)) second-phase particles in plate forms of 6061-T4 and 6061-T651 were not significantly different from those in plate forms of 2024-T351 and 7075-T651. The main differences were in the distribution of intermediate size (0.2 to 1 μm (0.08 × 10^{-4} to 0.4 × 10^{-4} in.)) particles. (Compare figs. 1(a), 2(a), 3, and 5.) Intermediate particles appeared to be more densely

and more homogeneously distributed in plate forms of 6061-T4 and 6061-T651 than in other alloys. Grain boundary segregation of particles was rarely observed in plate forms of 6061-T4 and 6061-T651 whereas in the other alloys, grain boundaries contained a high density of second-phase particles. In addition, bands containing high densities of second-phase particles were never observed in plate forms of 6061-T4 and 6061-T651. The more regular dimple formation in tensile and notch-bend specimens of 6061-T4 and 6061-T651 was attributed to the more homogeneous and denser distribution of void nucleating particles in the two alloys.

The 7075 and 7178 aluminum alloys examined in the present investigation were characterized by high densities of second-phase particles along grain boundaries and in bands aligned in the direction of rolling. Heterogeneity of particle distribution was considerably more pronounced in thick plates of the alloys than in thin sheets. (Compare fig. 3 with fig. 7(d) and fig. 5 with fig. 7(e).) The heterogeneous distribution of second phase particles influenced the fracture behavior of these alloys. As described in an earlier section, the fracture surfaces of plate tensile and precracked notch-bend specimens of the two alloys exhibited an abundance of relatively smooth facets (figs. 15, 16, 31(a), and 33(a)). The facets contained dimples nucleated at the finer second-phase particles and were interrupted by pockets containing large fractured particles. The facets were formed by extensive shearing and tearing. The facet dimensions were comparable with the grain size and with the spacing of particle bands. These features suggested that the fracturing process of thick specimens of 7075-T651 and 7178-T651 involved cracking of particles in bands and grain boundaries. Shearing and tearing of the areas between bands and boundaries followed. Also, as described in an earlier section, fractures of thick plate specimens of 7178-T651 exhibited a higher fraction of dimpled areas than did similar specimens of 7075-T651. (Compare, for example, figs. 31(a) and 33(a).) This difference would be expected because the higher density of coarse particles within the grains in 7178-T651 provide a greater number of sites for nucleation of microvoids and formation of dimples.

Thin sheets of aluminum alloys 2024, 7075, and 7178 exhibited considerably lower grain boundary segregation of particles and banding than did thick plates. This difference is evident when the microstructures of thick plate specimens of alloys in figures 1(a), 2(a), 3, and 5 are compared with the microstructures of thin sheets shown in figure 7. In addition, the plane stress condition was more conducive to dimple formation. Accordingly, smooth areas of the type observed on fracture surfaces of thick plate specimens were rare on tensile fractures of thin sheet specimens of the alloys. (Compare figs. 11 and 23.)

The segregation of second-phase particles at grain boundaries and along bands aligned in the rolling direction led also to the formation of secondary cracks and deep grooves along these boundaries and bands. The cracks propagated to considerable lengths in directions other than perpendicular to the direction of maximum tensile stress. Secondary cracks and grooves of the type described above can easily be seen in figures 15(a), 16, 23, 32, and 33(a).

Influence of Specimen Geometry and Type of Test on Fracture Morphology

The fracture morphology of aluminum alloys examined in the present investigation was strongly influenced by the type of test applied and specimen geometry. The influence of these variables was attributed mainly to their role in changing the state of stress causing fracture.

In the sheet tensile specimens of the alloys, deformation during testing occurred in a plane stress condition which was very conducive to formation of microvoids at the second-phase particles in the alloys. Accordingly, the primary failure mode was dimpled rupture (fig. 18). Dimples were equiaxed in regions of the specimens where a tensile stress component was predominant. Elongated dimples were observed on those regions of the fracture surfaces where a shear stress component was predominant. Although the fracture morphologies appeared to be similar in the different alloys at low magnifications in the scanning electron microscope (fig. 18), the differences between the alloys were revealed at higher magnifications (figs. 19, 22, and 23).

The fractures of sheet shear specimens of all alloys tested at the slower strain rate appeared to propagate mainly through matrices containing the fine second-phase particles (fig. 24). Large particles possibly influenced the process of fracture nucleation by cracking when the surrounding matrix was subjected to a large amount of plastic strain. Subsequent propagation of fracture occurred through the matrix. By far the most important factor influencing the shear fracture morphology appeared to be the shear stress state itself; differences in alloy compositions and microstructures had only minor effects. The shear fractures were so characteristic of the stress state that their morphology could be used to identify the regions representing failure along planes of high shear stress in tensile sheet specimens. One example of this behavior is illustrated in figure 20 for the tensile sheet specimen of aluminum alloy 2024-T3.

Differences in fracture morphology as a function of alloy type and microstructure were more obvious in thick plate sections than in thin sheets. (Compare figs. 11 and 18.) The thin sheet fractures of the different alloys both in shear and in tensile tests had more similarities than differences. The fractures of plate tensile specimens and precracked notch-bend specimens, however, exhibited morphologies characteristic of each alloy. The differences in fracture features were evident even at relatively low magnifications in the scanning electron microscope. Comparison of fracture morphology for thin sheets and thick plates revealed that some of the fracture surface features in thick plates were different from those in thin sheet specimens of the alloys, although there were similarities in the sizes and shapes of dimples on the fracture surfaces of thin sheets and thick plate specimens.

Strain Rate Effects on Fracture

The tensile plate and sheet specimens of the aluminum alloys examined in the present investigation were tested at three strain rate conditions, and the

shear tests were conducted at two different strain rates. The ultimate tensile strengths are listed in table V for sheet and plate specimens of the alloys tested at various strain rates. The tensile strength varied little as a function of strain rate. Fracture morphology of the alloys was also similar for the different strain rates in tension tests. The shear strength of the alloys, both for the longitudinal and the transverse orientations, was reduced substantially when the strain rate was raised (table VI). With increase in strain rate, the shear strengths of 2024-T3, 7075-T6, and 7178-T6 were reduced by 42 to 56 percent whereas those of 6061-T4 and 6061-T6 showed reductions of 21 to 26 percent. The shear fracture morphology did not change substantially with increase in strain rate in alloys 6061-T4 and 6061-T6, but differences were noted between the slow and fast strain rate fractures of alloys 2024-T3, 7075-T6, and 7178-T6. The shear fractures of these latter alloys showed a somewhat rougher morphology for the fast strain rate, and fracture surfaces exhibited a greater fraction of cracked second-phase particles. These conditions are illustrated for alloy 7075-T6 in figure 34 by scanning electron fractographs of specimens tested at the slow and fast strain rates.

Recall that the sheet specimens of alloys 2024-T3, 7075-T6, and 7178-T6 exhibited heterogeneous particle distributions with greater segregation and banding of large particles than observed in sheet specimens of 6061-T4 and 6061-T6. Therefore, the effect of strain rate on shear fracture morphology is related possibly to the degree of particle segregation in the alloys. A greater fraction of large particles may crack when shear specimens of alloys are tested at the fast strain rate than when they are tested at the slow strain rate. This would result in a reduction of the effective area carrying the load and in turn lead to fracture at lower loads. The reduced ultimate shear strength at the high strain rate and the occurrence of greater fraction of large cracked particles on fast strain rate fractures support this hypothesis. However, only a limited amount of work has been reported in the literature on shear fracture mechanisms in aluminum alloys, and additional investigations are needed to relate second-phase particle distribution and shear fracture morphology.

CONCLUDING REMARKS

The microstructure and the time-independent room temperature fracture behavior were examined in thin sheets and thick plates of structural aluminum alloys 2024, 6061, 7075, and 7178 in selected heat treatments. Several different fracture morphologies were identified and were related to microstructural features.

Microstructures of the alloys were characterized by elongated grains and dense distributions of second phase particles. Particle chemical compositions, sizes, and distributions were different in the alloys and were dependent on the form of commercial product (sheet or plate). Chemical analysis of particles using energy dispersive X-ray (edax) and associated scanning electron microscopy showed that several types of second-phase particles were present in the alloys. Among these, some particles such as $CuAl_2$, $CuMgAl_2$, Mg_2Si, and (Cu, Fe, Mn) Al_6 have been reported by other investigators. The present investigation also showed the presence of several particles containing various amounts of Si, Fe, Mn, and Cr that have not been reported in the published literature.

Examination of fracture morphology of thick plate tensile and precracked notch-bend specimens showed several cracked particles and predominantly dimpled fractures in alloys 2024-T351, 6061-T4, and 6061-T651. The sizes and shapes of dimples were dependent on the precipitate distribution in the alloys. Plate tensile and notch-bend specimens of 7075-T651 and 7178-T651 exhibited cracked particles and an abundance of relatively smooth facets on their fracture surfaces. The facets were apparently formed by extensive shearing and tearing in areas between grain boundaries and bands of second-phase particles.

Sheet tensile specimens of all alloys exhibited cracked particles and dimpled fractures with only small differences in the dimple characteristics between the alloys. Thin sheet shear specimens of all alloys exhibited relatively smooth fracture morphologies with large portions of the fractures propagating through the alloy matrices containing fine precipitates. Elongated and shallow dimples and cracked particles were found on fracture surfaces of shear specimens.

Microstructural variables including grain structure and second-phase particle distribution influenced fracture morphology, particularly for thick specimens. The type of loading (tensile, shear, or notch-bend) also had a signficant effect on fracture morphology. The specimen orientation examined in the present investigation had only minor influences on fracture behavior.

Tensile strength and fracture morphology were independent of the test strain rate over two to three orders of magnitude. One to two orders of magnitude of higher strain rate resulted in 21 to 26 percent lower shear strengths of aluminum alloys 6061-T4 and 6061-T6 whereas the shear fracture morphology was not affected. A similar rise in strain rate led to lower shear strengths of 2024-T3, 7075-T6, and 7178-T6 (42 to 56 percent) and the lowering of shear strength was accompanied by increasingly rough fracture surfaces which also exhibited greater densities of second-phase particles. Second-phase particle cracking was proposed as the mechanism responsible for low shear strength at high strain rates.

In analyzing service failures that occur under complex conditions, characteristic features of the type described in this paper should prove useful for establishing the mechanisms and causes of failure.

Langley Research Center
National Aeronautics and Space Administration
Hampton, VA 23665
November 18, 1977

APPENDIX A

SHEAR TEST PROCEDURE

The type of shear specimen used in the present investigation has been recommended by the Aerospace Industries Association (refs. 17 and 18) and is shown in figure A1. The specimen was loaded in axial tension, which resulted in shearing stresses with negligible normal stresses in the central area between the slots. Specimens were tested at cross-head displacement rates of 2.54 mm/min (0.1 in./min) and 76.2 mm/min (3 in./min).

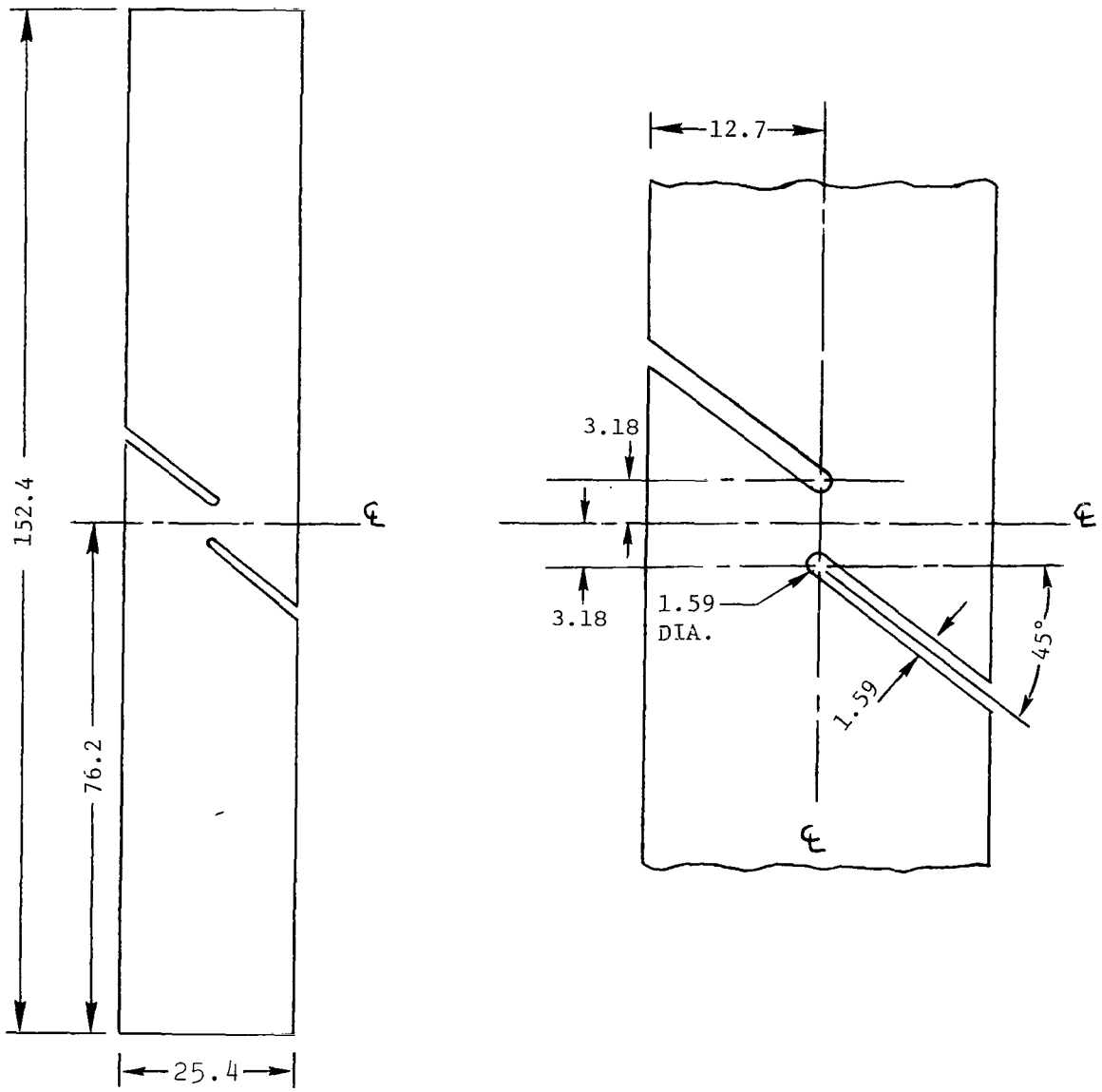

Figure A1.- Thin sheet shear specimen. All dimensions in mm (in.) unless otherwise noted. Nominal sheet thickness 1 mm (1 mm = 3.94×10^{-2} in.).

APPENDIX B

NOTCH-BEND TEST PROCEDURE

The notch-bend specimen used in the present investigation was of nominal dimensions 152.4 mm (6 in.) by 25.4 mm (1 in.) by 12.7 mm (0.5 in.) and is shown in figure B1. A fatigue crack was induced at the root of the machined notch and the specimen was then fractured under monotonic loading. The monotonic load was applied in three-point bending with a span of 101.6 mm (4 in.) between supports. Specimens were tested with longitudinal and transverse orientations and with the crack propagation direction in the short transverse direction. The maximum stress intensity factor for failure K_{IQ} was calculated from

$$K_{IQ} = Y \frac{6Ma^{1/2}}{Bw^2}$$

where

M maximum value of bending moment causing failure, N-mm (lb-in.)

a crack length (length of machined slot plus fatigue crack), mm (in.)

w specimen width, 25.4 mm (1 in.)

B specimen thickness, 12.7 mm (0.5 in.)

The factor Y is a compliance calibration factor. For the specimen used in the present investigation:

$$Y = 1.93 - 3.07\left(\frac{a}{w}\right) + 14.53\left(\frac{a}{w}\right)^2 - 25.11\left(\frac{a}{w}\right)^3 + 25.80\left(\frac{a}{w}\right)^4$$

(See ref. 19.)

APPENDIX B

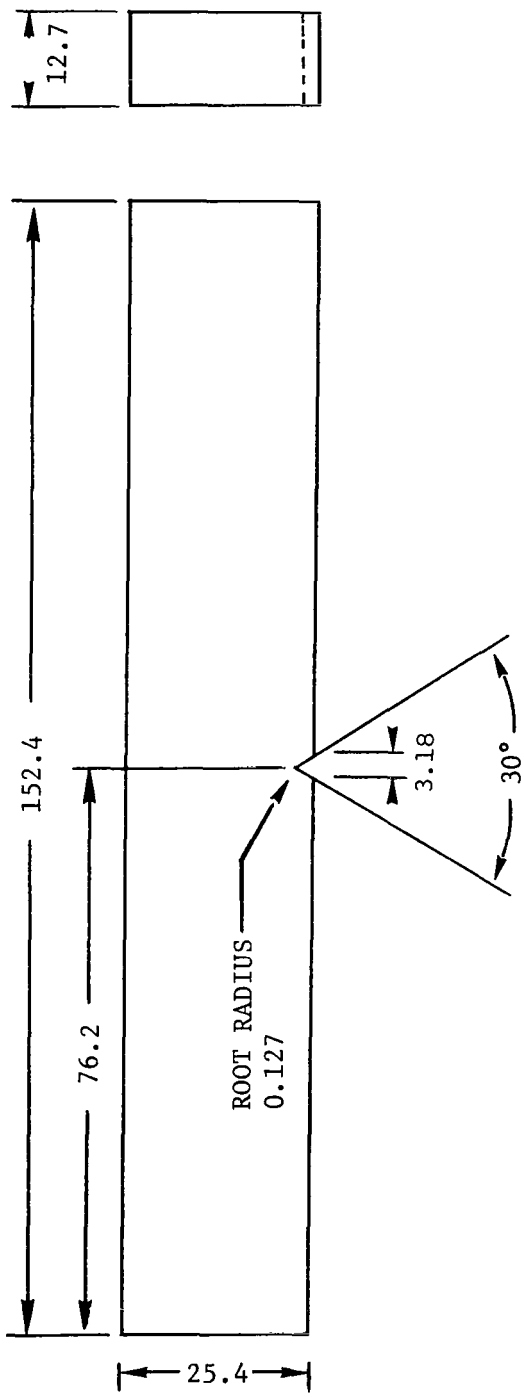

Figure B1.- Notch-bend test specimen. All dimensions are in mm (in.) unless otherwise noted (1 mm = 3.94×10^{-2} in.).

APPENDIX C

CHEMICAL ANALYSIS OF SECOND PHASE PARTICLES

Scanning electron microscopy and associated energy dispersive X-ray analysis (edax) were used in the present investigation for chemical analysis of second-phase particles in aluminum alloys. The edax patterns are X-ray intensity counts plotted against the energy of the X-rays emitted from the phase being analyzed.

In second-phase particle analysis by the edax technique, the edax pattern may contain a matrix contribution. This contribution results when the electron beam focused on a particle irradiates a volume that includes not only the particle but also the surrounding matrix, and thus leads to X-ray emission from both the particle and the matrix. In the present investigation, matrix contribution includes the contribution not only of the aluminum matrix containing elements in solid solution but also of the aging precipitates that are too fine to be observed in the scanning electron microscope.

Determination of the particle chemistry, even qualitatively, is difficult under conditions where matrix contribution is possible. In the present investigation, the problem was partly solved by a normalizing procedure.

Figure C1(a) shows a scanning electron fractograph obtained from a notch-bend specimen of aluminum alloy 7075-T651. The particle marked A in the figure was analyzed as described below.

TABLE C1.- EDAX INTEGRATED INTENSITIES FOR PARTICLE AND MATRIX

	Integrated intensity counts	
Element	Particle pattern	Matrix pattern
Mg	6 165	842 (no peak)
Al	12 963	12 947
Si	4 399	305 (no peak)
Cu	167	175
Zn	367	366

First, an edax pattern was obtained by focusing the electron beam on the particle. The intensity peaks in the pattern were identified and integrated intensity counts were noted for the peaks. The pattern is shown in figure C1(b), and the integrated counts for the elements Mg, Al, Si, Cu, and Zn are listed in the column "Particle pattern" in table C1. A second edax pattern was obtained by focusing the electron beam on a matrix area adjacent to the particle and per-

forming the analysis until the matrix edax pattern developed the same integrated intensity as the particle edax pattern for a minor constituent observed in the particle pattern. Figure C1(c) shows a matrix edax pattern which was obtained so that the integrated intensity for Zn was the same as that obtained in the particle pattern. The integrated intensity counts for the elemental peaks in figure C1(c) are listed in the column "Matrix pattern" in table C1. When absorption effects are neglected, the intensity peaks of elements in the matrix edax pattern of figure C1(c) represent those that would be generated for a volume of matrix irradiated material only (no precipitate or particle irradiation) containing the same amount of Zn as was observed for the particle irradiated volume analyzed in figure C1(b). Subtracting the integrated intensity counts of the elements in the column "Matrix pattern" from the counts of the same elements in the column "Particle pattern" shows that particle A in figure C1(a) contained only Mg and Si and that the Al, Cu, and Zn peaks in figure C1(b) resulted from matrix contributions. An accurate quantitative chemical analysis cannot be obtained by the technique described in this appendix because absorption effects are neglected.

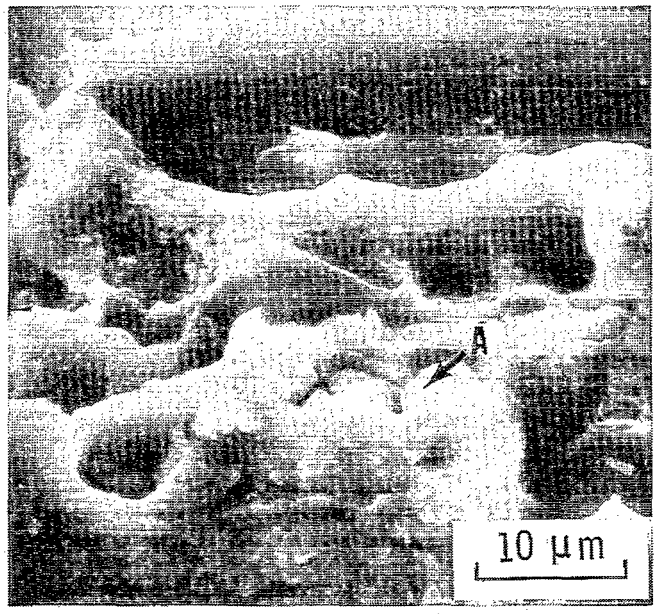

(a) Scanning electron fractograph.

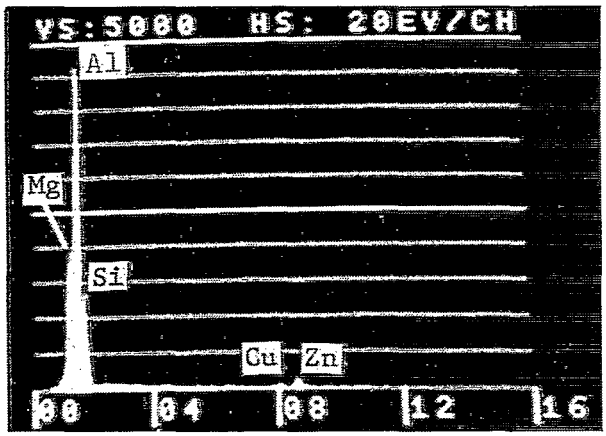

(b) Particle A.

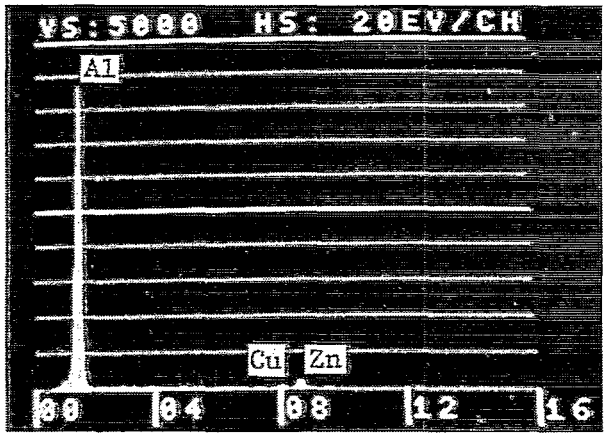

(c) Matrix.

L-77-335

Figure C1.- Scanning electron fractograph and edax intensity patterns obtained from notch-bend specimen of aluminum alloy 7075-T651 tested in longitudinal orientation. Numerals on horizontal scale are in keV. Bars on vertical scale indicate intensity in counts. (1 μm = 3.94×10^{-5} in.)

REFERENCES

1. Hunter, M. S.; and McMillan, J. C.: Fractography and Microstructure of Aluminum Alloys 7075-T651 and 7075-T7351. Electron Fractography, ASTM Special Tech. Publ. No. 436, American Soc. Testing and Materials, c.1968, pp. 196-211.

2. Unwin, P. N. T.; and Smith, G. C.: The Microstructure and Mechanical Properties of Al-6% Zn-3% Mg. J. Inst. Metals, vol. 97, Oct. 1969, pp. 299-310.

3. Singh, S. N.; and Flemings, M. C.: Influence of Ingot Structure and Processing on Mechanical Properties and Fracture of a High Strength Wrought Aluminum Alloy. Trans. Met. Soc., AIME, vol. 245, no. 8, Aug. 1969, pp. 1811-1819.

4. Tanaka, J. P.; Pampillo, C. A.; and Low, J. R., Jr.: Fractographic Analysis of the Low Energy Fracture of an Aluminum Alloy. Review of Developments in Plane Strain Fracture Toughness Testing, ASTM Special Tech. Publ. 463, c.1970, pp. 191-269.

5. Kirman, I.: The Relation Between Microstructure and Toughness in 7075 Aluminum Alloy. Metall. Trans., vol. 2, July 1971, pp. 1761-1770.

6. Low, J. R., Jr.; VanStone, R. H.; and Merchant, R. H.: An Investigation of Plastic Fracture in Aluminum Alloy. NASA CR-131100, 1972.

7. Peel, C. J.; Wilson, R. N.; and Forsyth, P. J. E.: Relationships Between Some Microstructural Features and the Fracture Toughness of an Al-Zn-Mg-Cu-Mn Forging Alloy. Met. Sci. J., vol. 6, May 1972, pp. 102-106.

8. Broek, D.: The Role of Inclusions in Ductile Fracture and Fracture Toughness. Eng. Fracture Mech., vol. 5, no. 1, Feb. 1973, pp. 55-66.

9. Rosenfield, A. R.; Price, C. W.; Martin, C. J.; Thompson, D. S.; and Zinkham, R. E.: Research on Synthesis of High Strength Aluminum Alloys. Part I. The Relation Between Precipitate Microstructure and Mechanical Properties in Aluminum Alloys. AFML-TR-74-129, Part I, U.S. Air Force, Dec. 1974. (Available from DDC as AD/A 002 875.)

10. Metals Handbook. Vol. 9 - Fractography and Atlas of Fractographs. American Soc. Metals, c.1974.

11. Hahn, G. T.; and Rosenfield, A. R.: Metallurgical Factors Affecting Fracture Toughness of Aluminum Alloys. Metall. Trans. A, vol. 6A, Apr. 1975, pp. 653-668. (Discussion, pp. 668-670.)

12. Metric Practice Guide. E380-72, American Soc. Testing & Mater., June 1972.

13. Van Horn, Kent R., ed.: Aluminum. Vol. I - Properties, Physical Metallurgy and Phase Diagrams. American Soc. Metals, c.1967.

14. Metals Handbook. Vol. 7 - Atlas of Microstructures of Industrial Alloys. American Soc. Metals, c.1972.

15. Featherby, Michael: Fractography of Advanced Composites and High Strength Aluminum. CASD-ERR-73-049, Convair/General Dynamics, Dec. 1973.

16. Fine, M. E.: Precipitation Hardening of Aluminum Alloys. Metall. Trans. A, vol. 6A, Apr. 1975, pp. 625-630.

17. Standard Elevated Temperature Testing Progress for Metallic Materials. Aerospace Industries Assoc. Standard Test Procedure, ARTC-13-5-1, July 1964.

18. Breindel, W. W.; Seale, C. L.; and Carlson, R. L.: Evaluation of a Single-Shear Specimen for Sheet Material. Proceedings ASTM, vol. 58, American Soc. Testing Materials, 1958, pp. 862-868.

19. Brown, William F., Jr.; and Srawley, John E.: Plane Strain Crack Toughness Testing of High Strength Metallic Materials. ASTM Special Tech. Publ. No. 410, c.1966.

TABLE I.- CHEMICAL COMPOSITIONS OF ALUMINUM ALLOYS INVESTIGATED

Element	Aluminum alloy compositions, weight, percent			
	2024	6061	7075	7178
Cu	3.8 to 4.9	0.15 to 0.40	1.2 to 2.0	1.6 to 2.4
Mg	1.2 to 1.8	.8 to 1.2	2.1 to 2.9	2.4 to 3.1
Zn	.25	.25	5.1 to 6.1	6.3 to 7.3
Si	.50	.4 to .8	.50	.50
Fe	.50	.70	.7	.7
Cr	.10	.15 to .35	.18 to .40	.18 to .40
Mn	.30 to .90	.15	.30	.30
Ti	----------	.15	.20	.20
Others	.15	.15	.15	.15
Al	Remainder	Remainder	Remainder	Remainder

TABLE II.- HEAT TREATMENTS AND MATERIALS SPECIFICATIONS OF ALUMINUM ALLOYS INVESTIGATED

Aluminum alloy	Product form	Heat treatment	Federal specification
2024	Sheet	T3	QQ-A-250/4d
2024	Plate	T351	QQ-A-250/4d
6061	Sheet and plate	T4	QQ-A-250/11d
6061	Sheet	T6	QQ-A-250/11d
6061	Plate	T651	QQ-A-250/11d
7075	Sheet	T6	QQ-A-250/12d
7075	Plate	T651	QQ-A-250/12d
7178	Sheet	T6	QQ-A-250/14d
7178	Plate	T651	QQ-A-250/14d

TABLE III.- MECHANICAL PROPERTIES OF ALUMINUM ALLOY THICK PLATES

Aluminum alloy	Orientation	0.2-percent offset yield strength,[a] MN/m^2 (ksi)	Ultimate tensile strength,[a] MN/m^2 (ksi)	Elongation in 50 mm (2 in.), percent	Maximum stress intensity,[b] $MN/m^{3/2}$ ($ksi\text{-}in^{1/2}$)
2024-T351	Longitudinal	422.7 (61.3)	501.3 (72.7)	20	39.6 (36)
	Transverse	369.6 (53.6)	484.0 (70.2)	18	36.3 (33)
6061-T4	Longitudinal	204.8 (29.7)	255.8 (37.1)	26	---- (----)
	Transverse	200.6 (29.1)	277.2 (40.2)	22	33.0 (30)
6061-T651	Longitudinal	305.4 (44.3)	317.9 (46.1)	22	44.0 (40)
	Transverse	302.7 (43.9)	328.2 (47.6)	16	44.0 (40)
7075-T651	Longitudinal	557.1 (80.8)	594.3 (86.2)	12	41.2 (37.5)
	Transverse	539.2 (78.2)	595.0 (86.3)	13	[b]36.3 (33)
7178-T651	Longitudinal	588.8 (85.4)	636.4 (92.3)	11	[b]28.6 (26)
	Transverse	564.0 (81.8)	619.2 (89.8)	11	[b]23.1 (21)

[a]Tensile tests performed at strain rate of 0.005/min; 0.05/min.

[b]Maximum K_{IQ} values; specimens meet American Society of Testing Materials thickness requirement for valid K_{IC}. ($K_{IQ} = K_{IC}$ at this thickness requirement.)

TABLE IV.- TENSILE PROPERTIES OF ALUMINUM ALLOY THIN SHEETS

Aluminum alloy	Orientation	0.2-percent offset yield strength, MN/m^2 (ksi)	Ultimate tensile strength, MN/m^2 (ksi)	Elongation in 50 mm (2 in.), percent
2024-T3	Longitudinal	362.0 (52.5)	499.9 (72.5)	24
	Transverse	313.7 (45.5)	475.7 (69.0)	27
6061-T4	Longitudinal	180.0 (26.1)	281.3 (40.8)	27
	Transverse	170.3 (24.7)	275.8 (40.0)	30
6061-T6	Longitudinal	300.6 (43.6)	331.0 (48.0)	22
	Transverse	284.8 (41.3)	324.7 (47.1)	16
7075-T6	Longitudinal	518.5 (75.2)	566.8 (82.2)	23
	Transverse	588.1 (85.3)	663.3 (96.2)	17
7178-T6	Longitudinal	568.1 (82.4)	617.1 (89.5)	19
	Transverse	550.2 (79.8)	635.7 (92.2)	19

TABLE V.- ULTIMATE TENSILE STRENGTH OF ALUMINUM ALLOYS

AT VARIOUS STRAIN RATES

Aluminum alloy	Product form	Specimen orientation	Ultimate tensile strength, MN/m^2 (ksi), for strain rate of -		
			0.005/min	0.005/min; 0.05/min[a]	1.5/min
2024-T3	Sheet	Longitudinal	496.4 (72.0)	499.9 (72.5)	493.0 (71.5)
2024-T3	Sheet	Transverse	482.6 (70.0)	475.7 (69.0)	466.1 (67.6)
2024-T351	Plate	Longitudinal	505.4 (73.3)	501.9 (72.8)	491.6 (71.3)
2024-T351	Plate	Transverse	488.8 (70.9)	486.8 (70.6)	477.8 (69.3)
6061-T4	Sheet	Longitudinal	282.0 (40.9)	281.3 (40.8)	277.9 (40.3)
6061-T4	Sheet	Transverse	279.2 (40.5)	276.5 (40.1)	273.0 (39.6)
6061-T4	Plate	Longitudinal	253.0 (36.7)	254.4 (36.9)	250.3 (36.3)
6061-T4	Plate	Transverse	274.4 (39.8)	274.4 (39.8)	272.3 (39.5)
6061-T6	Sheet	Longitudinal	336.5 (48.8)	329.6 (47.8)	331.0 (48.0)
6061-T6	Sheet	Transverse	326.1 (47.3)	324.7 (47.1)	324.7 (47.1)
6061-T651	Plate	Longitudinal	316.5 (45.9)	317.2 (46.0)	315.8 (45.8)
6061-T651	Plate	Transverse	328.9 (47.7)	329.6 (47.8)	327.5 (47.5)
7075-T6	Sheet	Longitudinal	569.5 (82.6)	566.8 (82.2)	568.1 (82.4)
7075-T6	Sheet	Transverse	665.3 (96.5)	667.4 (96.8)	653.6 (94.8)
7075-T651	Plate	Longitudinal	591.6 (85.8)	591.6 (85.8)	586.1 (85.0)
7075-T651	Plate	Transverse	610.9 (88.6)	595.0 (86.3)	585.4 (84.9)
7178-T6	Sheet	Longitudinal	627.4 (91.0)	621.9 (90.2)	606.7 (88.0)
7178-T6	Sheet	Transverse	634.3 (92.0)	635.7 (92.2)	624.0 (90.5)
7178-T651	Plate	Longitudinal	633.6 (91.9)	632.9 (91.8)	635.0 (92.1)
7178-T651	Plate	Transverse	613.6 (89.0)	618.5 (89.7)	613.6 (89.0)

[a]0.005/min to yield followed by 0.05/min to failure.

TABLE VI.- ULTIMATE SHEAR STRENGTHS OF ALUMINUM ALLOY THIN SHEETS

[Gage lengths varied between 4.27 mm (0.1680 in.) and 4.57 mm (0.1801 in.)]

Alloy	Cross-head speed designation	Ultimate shear strength, MN/m^2 (ksi)	
		Longitudinal	Transverse
2024-T3	2.54 mm/min (0.1 in./min)	355.8 (51.6)	356.7 (51.8)
	76.2 mm/min (3 in./min)	198.5 (28.8)	207.3 (30.1)
6061-T4	2.54 mm/min (0.1 in./min)	216.6 (31.4)	215.8 (31.3)
	76.2 mm/min (3 in./min)	167.3 (24.3)	169.7 (24.6)
6061-T6	2.54 mm/min (0.1 in./min)	235.0 (34.1)	239.1 (34.7)
	76.2 mm/min (3 in./min)	174.3 (25.3)	185.1 (26.8)
7075-T6	2.54 mm/min (0.1 in./min)	401.1 (58.2)	405.4 (58.8)
	76.2 mm/min (3 in./min)	177.6 (25.8)	185.8 (27.0)
7178-T6	2.54 mm/min (0.1 in./min)	424.4 (61.6)	443.0 (64.3)
	76.2 mm/min (3 in./min)	209.5 (30.4)	202.9 (29.4)

TABLE VII.- INDEX OF MICROSTRUCTURE INCLUDING SECOND-PHASE PARTICLE ANALYSIS AND FRACTURE MORPHOLOGY FOR ALLOYS, HEAT TREATMENTS, PRODUCT FORMS, AND TEST SPECIMENS AS INDICATED

Alloy and heat treatment	Product form	Test specimen	Reference figures and description	
			Microstructure and second phase particle analysis, figure number	Fracture morphology, figure number
2024-T3	Sheet	Tensile	7	18, 19, 20
2024-T3	Sheet	Shear	7	24, 25
2024-T351	Plate	Tensile	1	11, 12
2024-T351	Plate	Notch-bend	1	27, 28
6061-T4	Sheet	Tensile	7	18, 21, 22
6061-T4	Sheet	Shear	7	24
6061-T4	Plate	Tensile	2	11, 13
6061-T4	Plate	Notch-bend	2	29
6061-T6	Sheet	Tensile	7	18, 21, 22
6061-T6	Sheet	Shear	7	24
6061-T651	Plate	Tensile	2	11, 14
6061-T651	Plate	Notch-bend	2	29, 30
7075-T6	Sheet	Tensile	7, 8	18, 23
7075-T6	Sheet	Shear	7	24, 34
7075-T651	Plate	Tensile	3, 4	11, 15
7075-T651	Plate	Notch-bend	3, 4	31, 32
7178-T6	Sheet	Tensile	7, 9	18, 23
7178-T6	Sheet	Shear	7, 10	24, 26
7178-T651	Plate	Tensile	5, 6	11, 16, 17
7178-T651	Plate	Notch-bend	5, 6	33

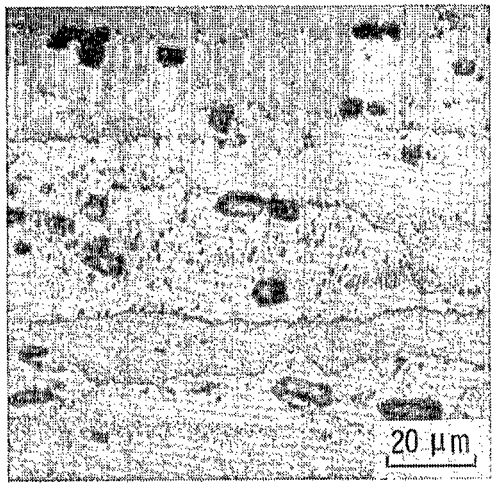

(a) Longitudinal section.

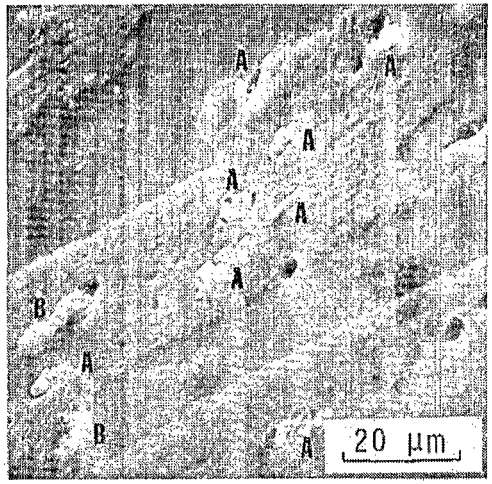

(b) Transverse section.

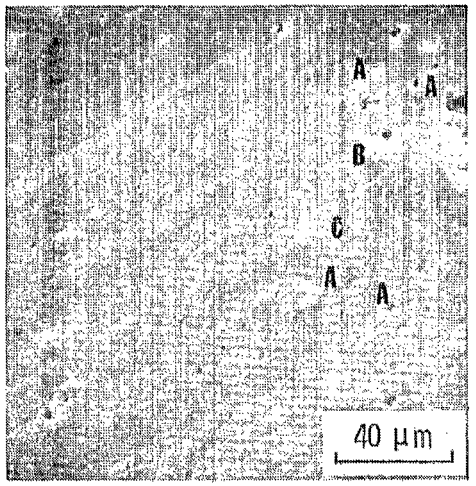

(c) Transverse section.

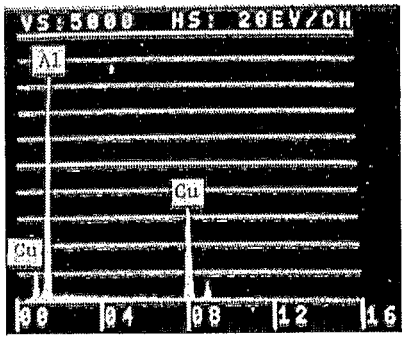

(d)

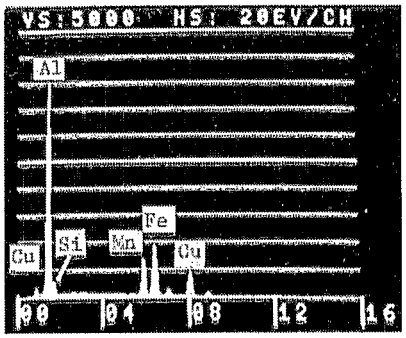

(e)

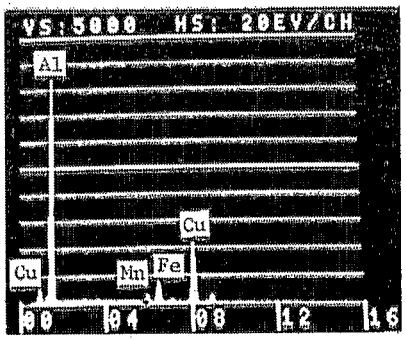

(f)

L-33-336

Figure 1.- Optical micrograph (a) and scanning electron micrographs (b) and (c) of a 2024-T351 plate specimen. Energy dispersive X-ray analysis (edax) patterns from second-phase particles A, B, and C are shown in (d), (e), and (f), respectively. Numerals on horizontal scale are in keV. Bars on vertical scale indicate intensity in counts. (1 µm = 3.94×10^{5} in.)

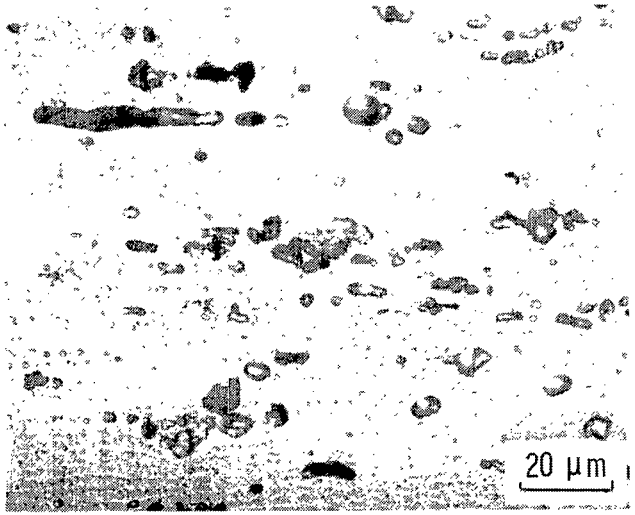

(a) Longitudinal section.

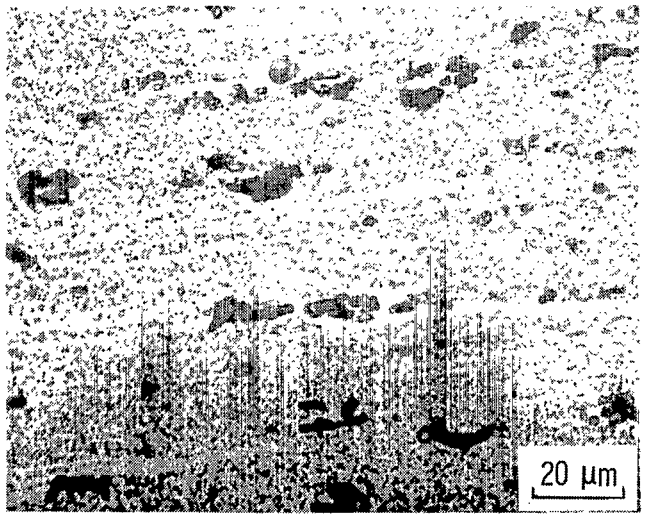

(b) Transverse section.

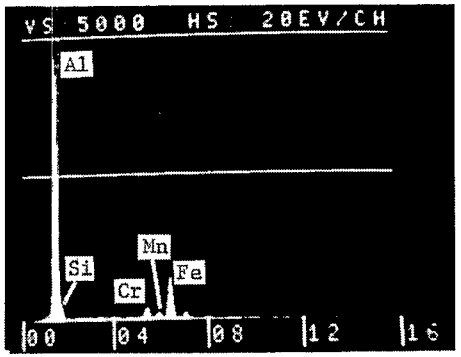

(c)

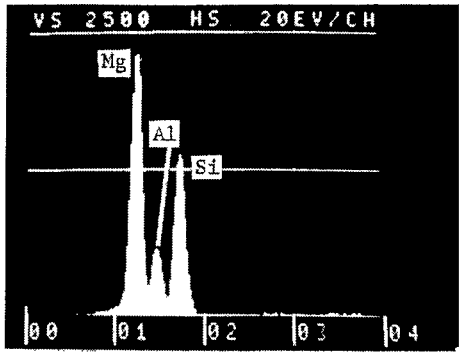

(d)

L-77-337

Figure 2.- Optical micrographs (a) and (b) and edax patterns of second-phase particles (c) and (d) from thick plate of aluminum alloys 6061-T4 and 6061-T651. Numerals on horizontal scale are in keV. Bars on vertical scale indicate intensity in counts. (1 µm = 3.94×10^{-5} in.)

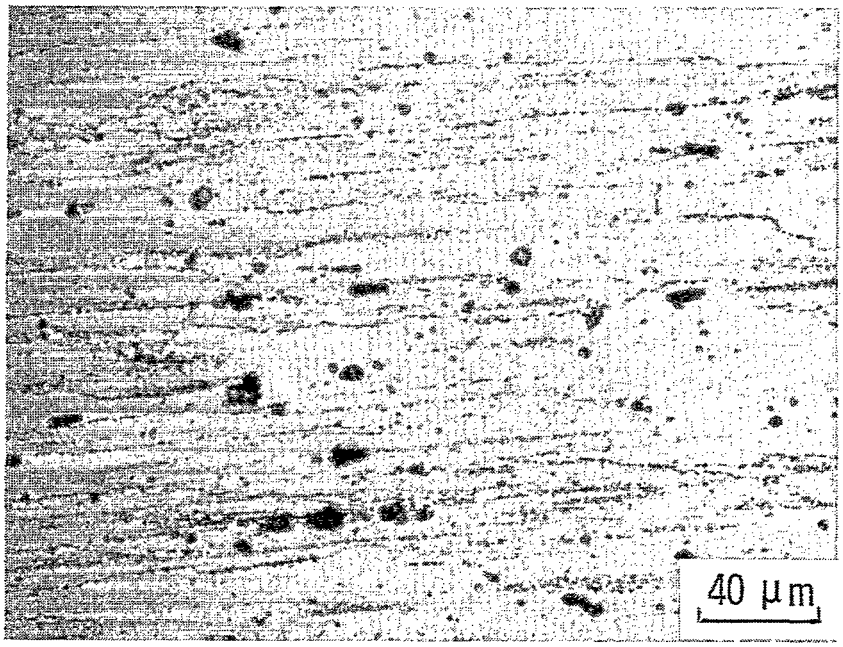

(a)

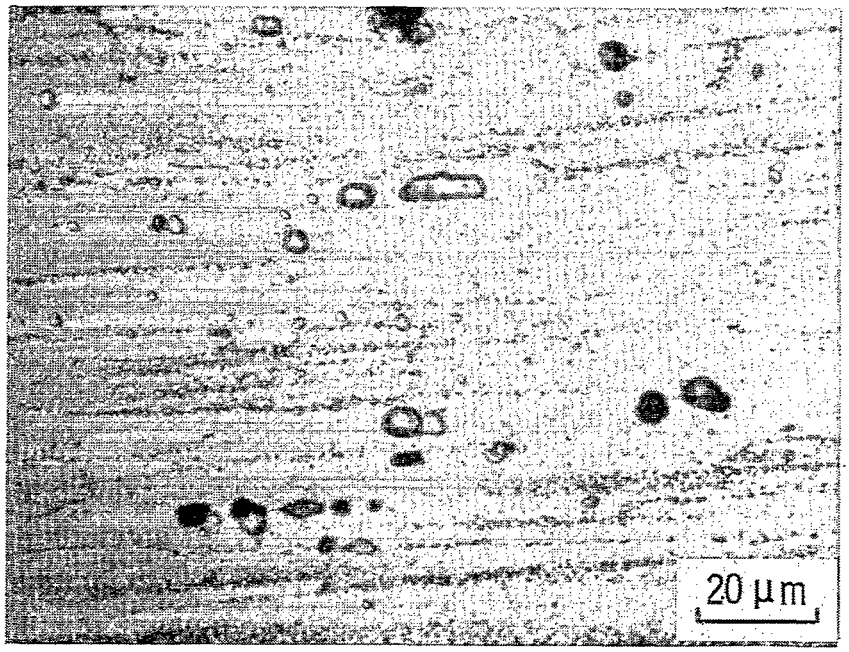

(b)

L-77-338

Figure 3.- Optical micrographs of aluminum alloy 7075-T651 longitudinal plate specimen. (1 µm = 3.94 × 10^{-5} in.)

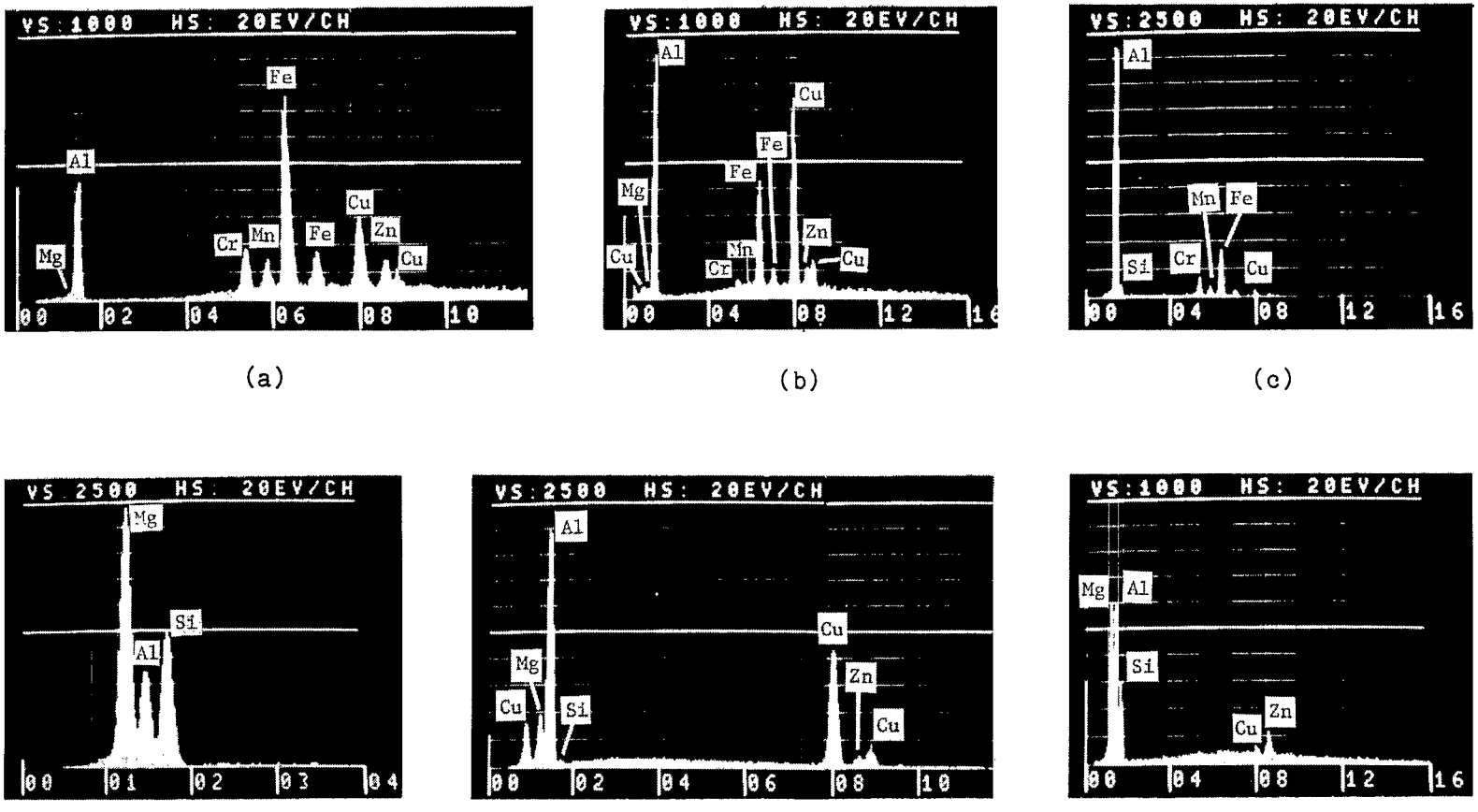

L-77-339

Figure 4.- Edax patterns for second-phase particles present in aluminum alloy 7075-T651 plate specimens. Numerals on horizontal scale are in keV. Bars on vertical scale indicate intensity in counts.

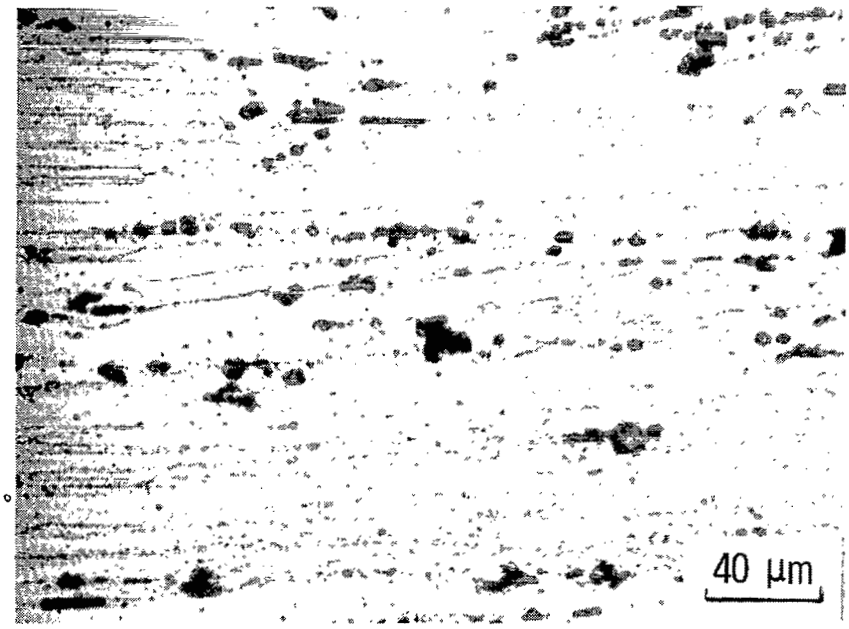

(a)

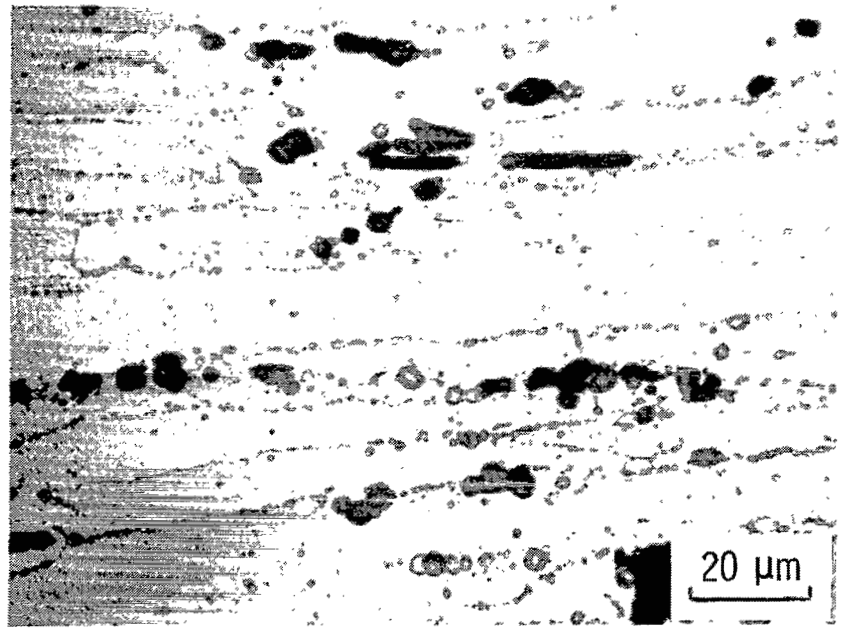

(b)

L-77-340

Figure 5.- Optical micrographs of aluminum alloy 7178-T651 transverse plate specimen. (1 μm = 3.94×10^{-5} in.)

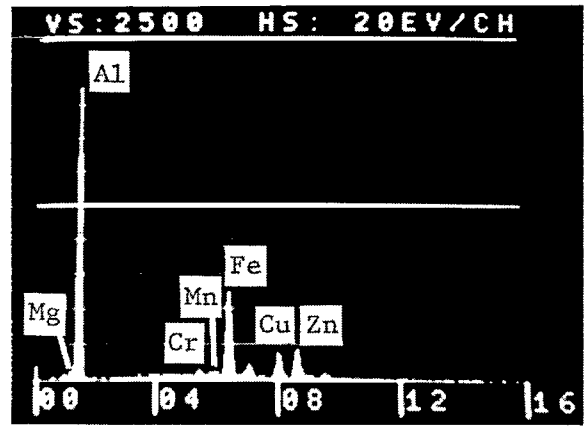

(a)

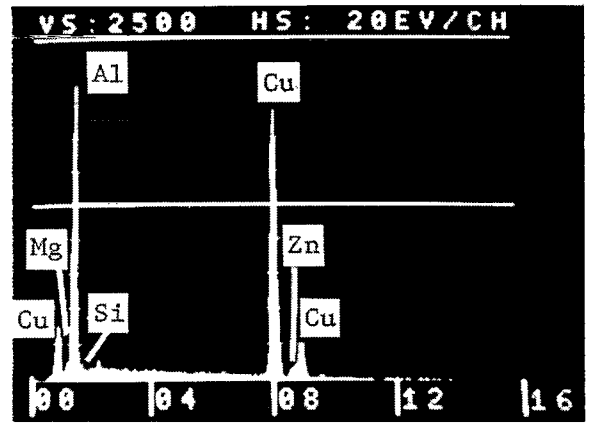

(b)

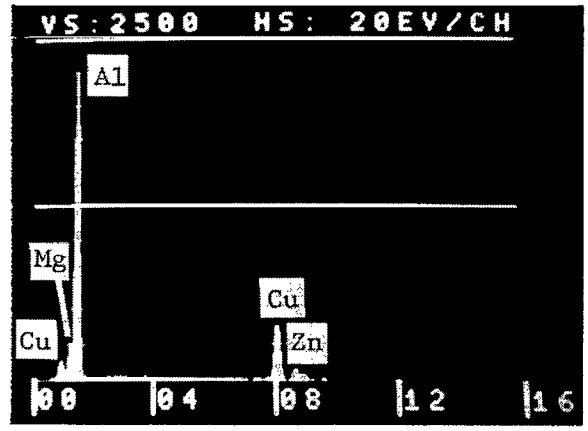

(c)

L-77-341

Figure 6.- Edax patterns for second phase particles present in aluminum alloy 7178-T651 plate specimens. Numerals on horizontal scale are in keV. Bars on vertical scale indicate intensity in counts.

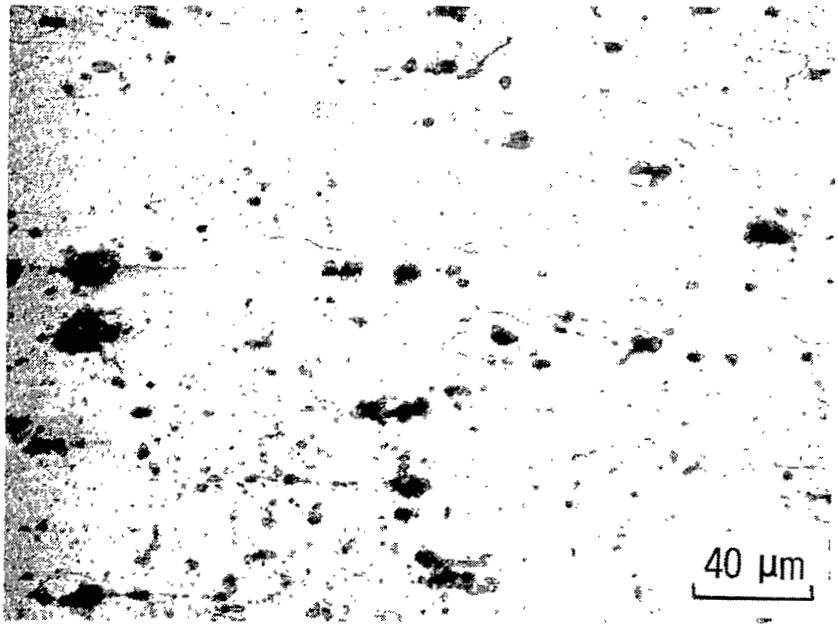

(a) 2024-T3.

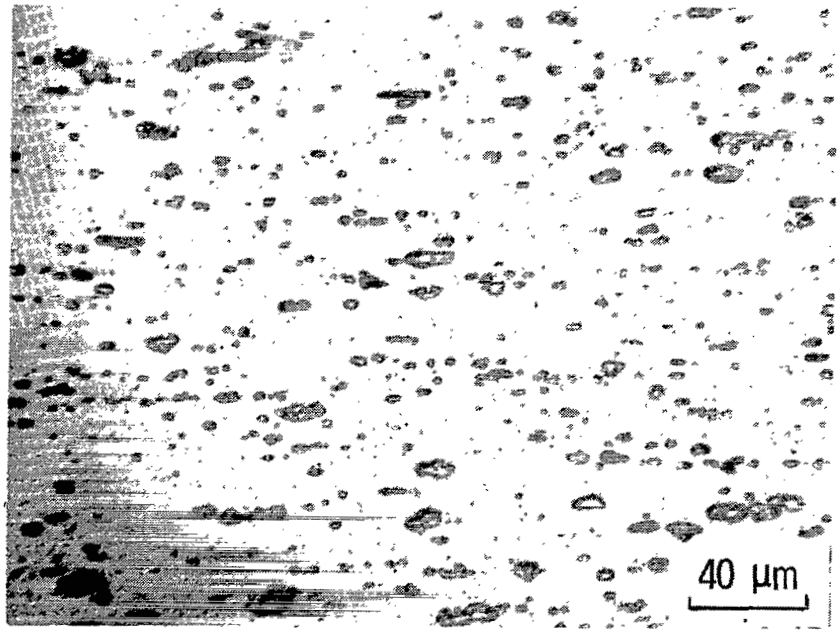

(b) 6061-T4.

L-77-342

Figure 7.- Optical micrographs of longitudinal sheet specimens of aluminum alloys investigated. (1 μm = 3.94×10^{-5} in.)

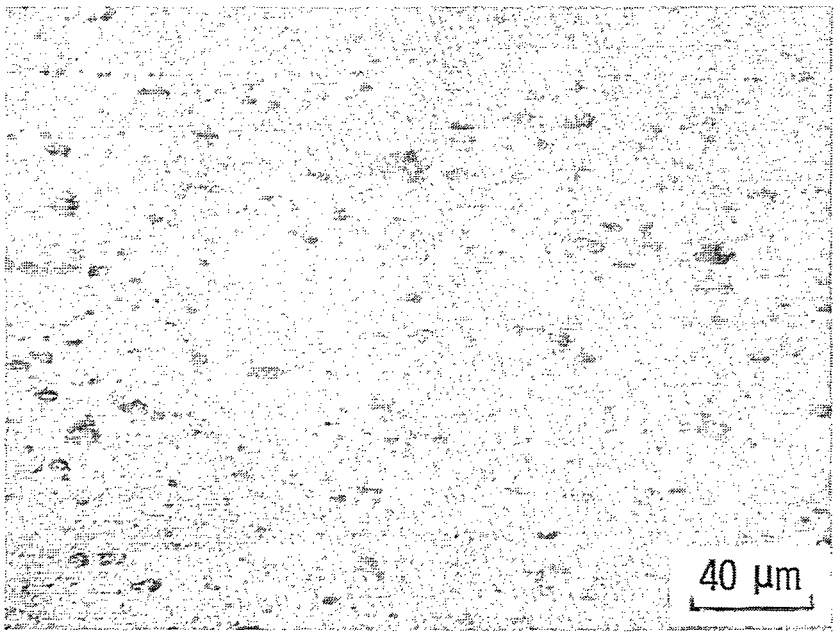

(c) 6061-T6.

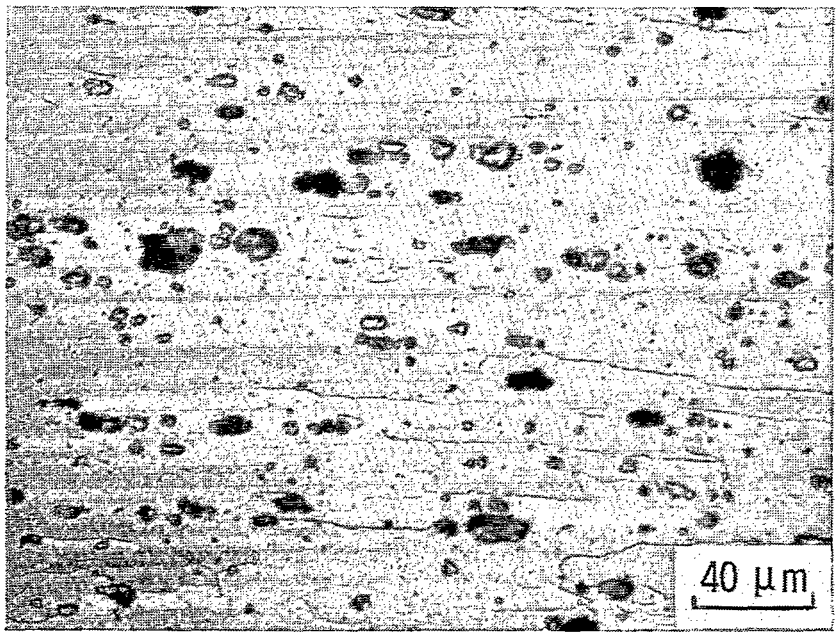

(d) 7075-T6.

L-77-343

Figure 7.- Continued.

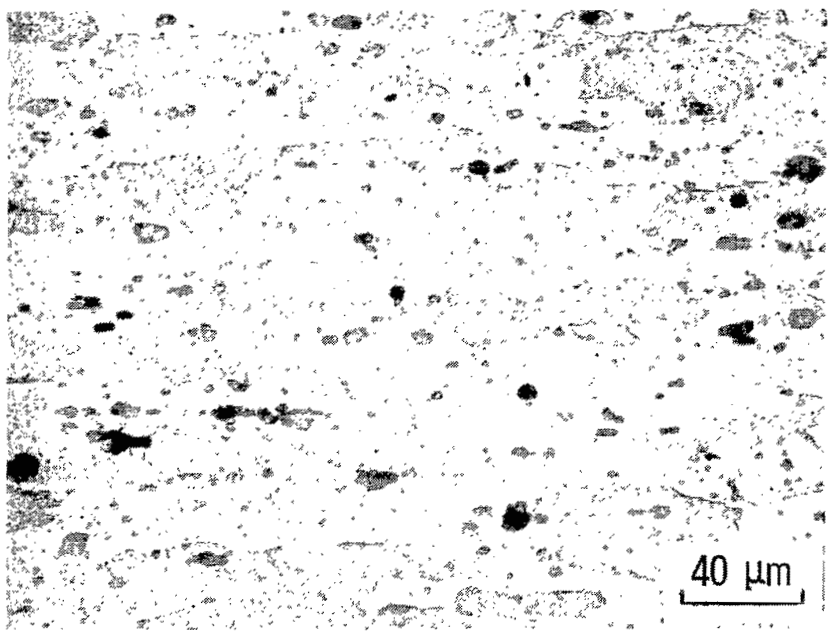

(e) 7178-T6.

Figure 7.- Concluded.

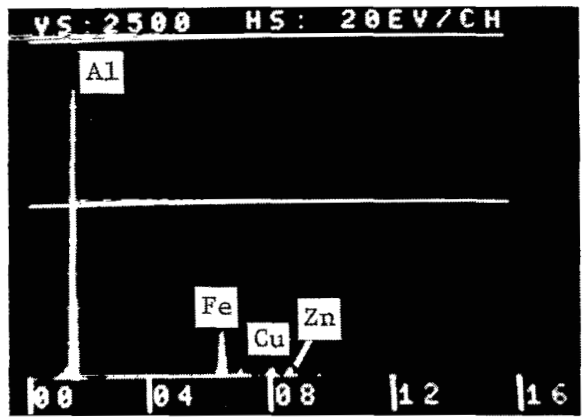

(a)

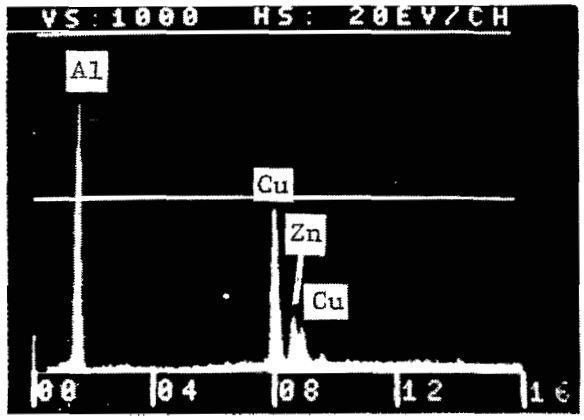

(b)

L-77-345

Figure 8.- Edax patterns for second-phase particles in 7075-T6 sheet tensile specimens. Numerals on horizontal scale are in keV. Bars on vertical scale indicate intensity in counts.

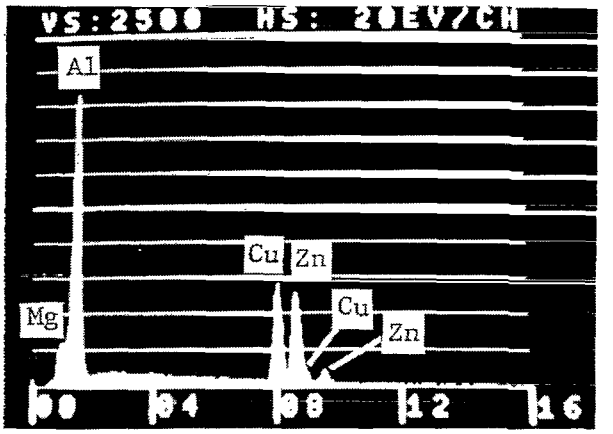

L-77-346

Figure 9.- Edax pattern for a type of second-phase particle observed on fracture surfaces of 7178-T6 sheet tensile specimens. Numerals on horizontal scale are in keV. Bars on vertical scale indicate intensity in counts.

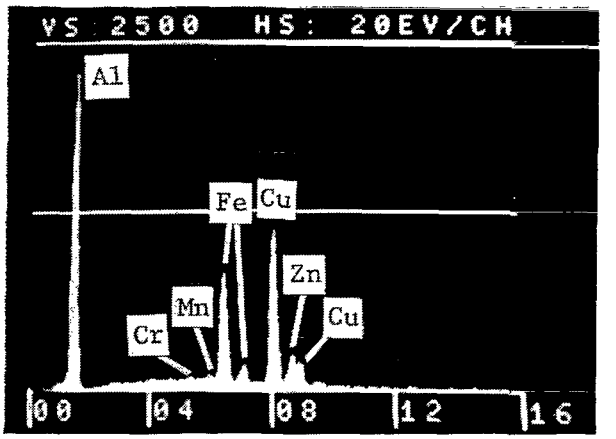

L-77-347

Figure 10.- Edax pattern for second-phase particles observed on fracture surfaces of 7178-T6 sheet shear specimens. Numerals on horizontal scale are in keV. Bars on vertical scale indicate intensity in counts.

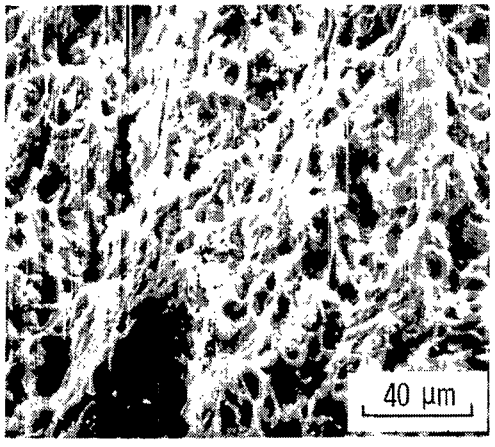

(a) 2024-T351 transverse specimen.

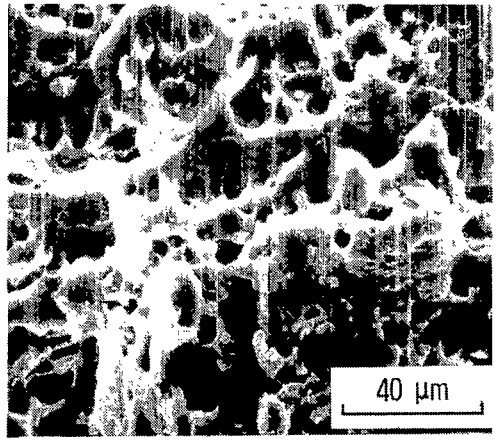

(b) 6061-T4 longitudinal specimen.

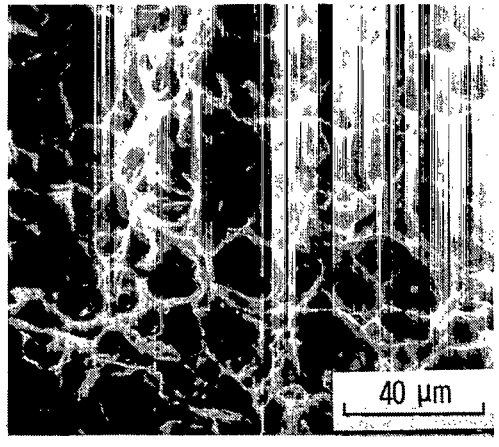

(c) 6061-T651 longitudinal specimen.

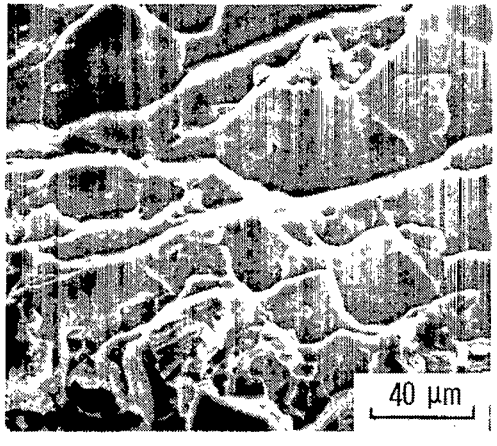

(d) 7075-T651 longitudinal specimen.

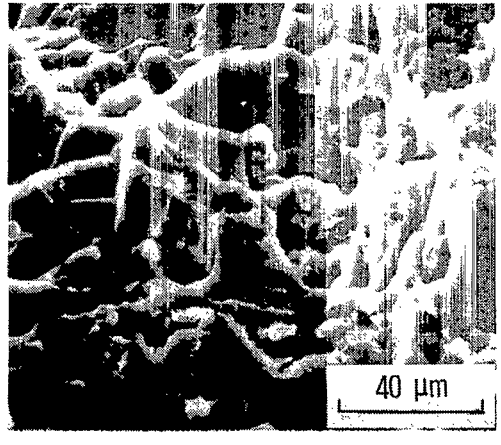

(e) 7178-T651 longitudinal specimen.

L-77-348

Figure 11.- Scanning electron fractographs of plate tensile specimens of aluminum alloys investigated. (1 μm = 3.94×10^{-5} in.)

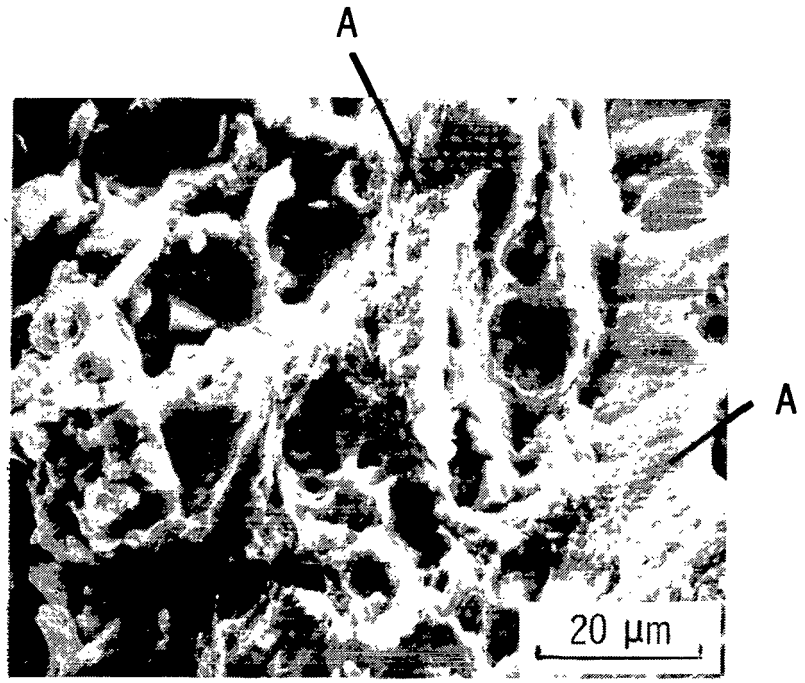

(a) Longitudinal specimen.

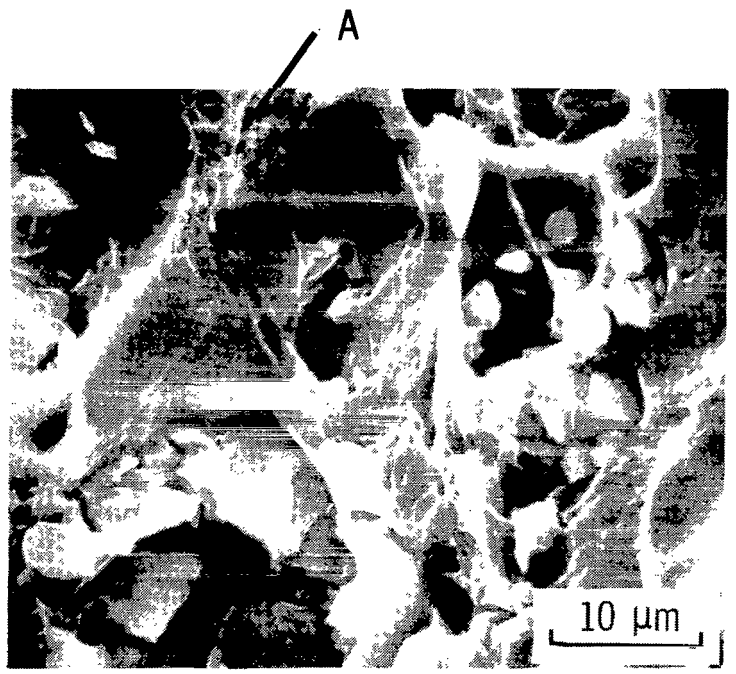

(b) Transverse specimen.

L-77-349

Figure 12.- Scanning electron fractographs of 2024-T351 plate tensile specimens. Areas labeled A identify fine dimples. (1 μm = 3.94×10^{-5} in.)

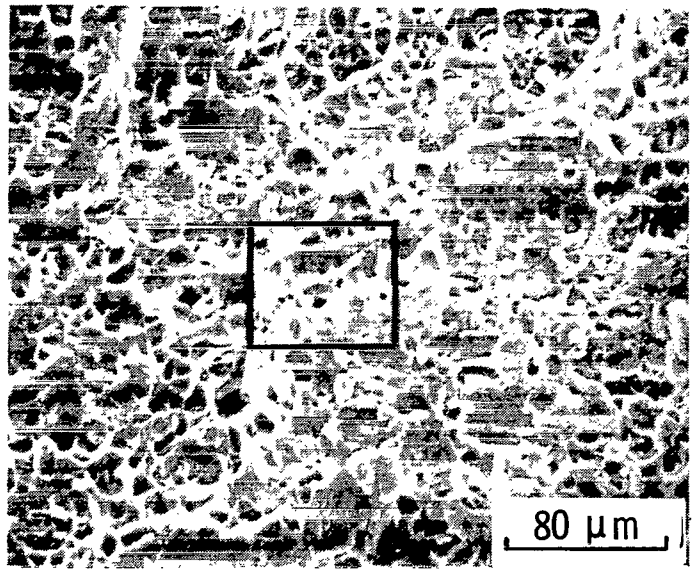

(a)

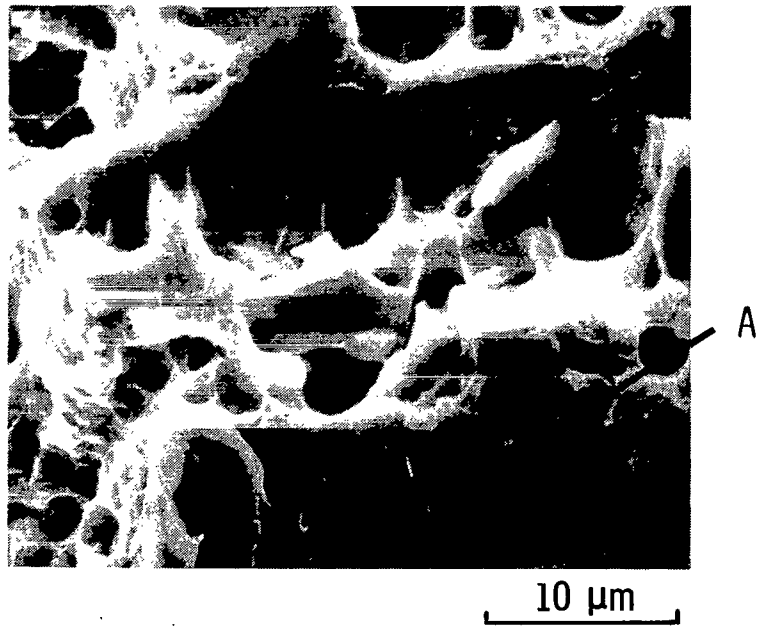

(b)

L-77-350

Figure 13.- Scanning electron fractographs of aluminum alloy 6061-T4 longitudinal plate tensile specimen. Fractograph in (b) was obtained by magnifying area marked in (a). Area labeled A identifies fine dimples. (1 µm = 3.94×10^{-5} in.)

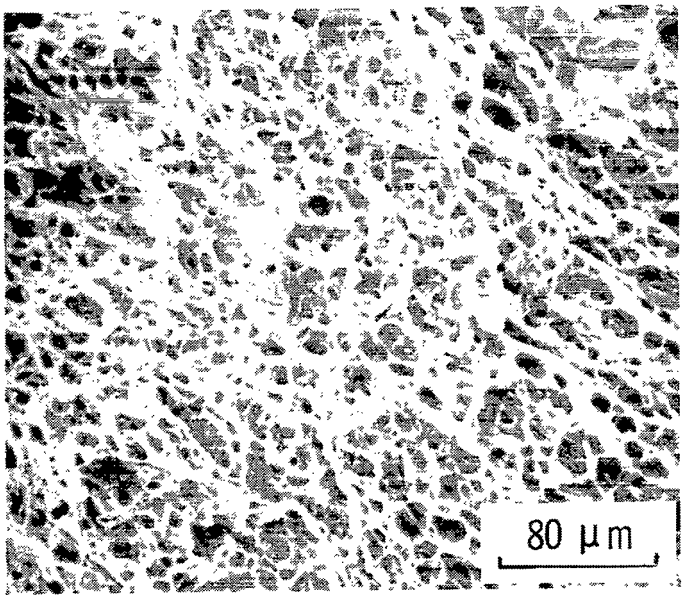

(a) Longitudinal specimen.

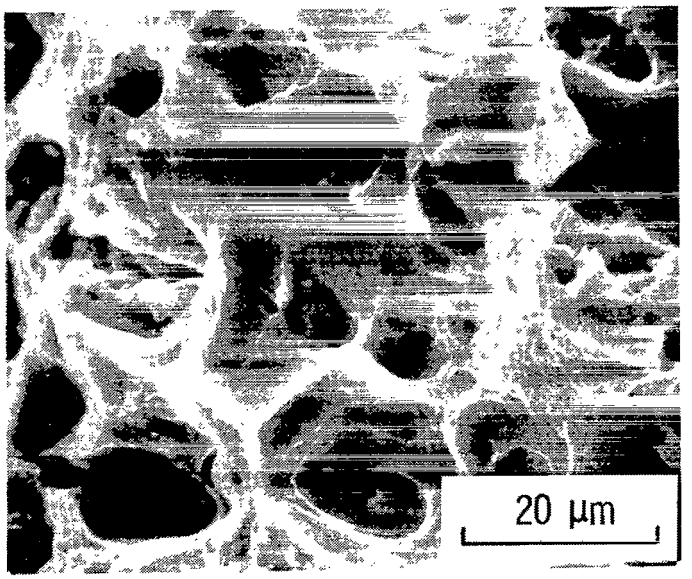

(b) Longitudinal specimen.

L-77-351

Figure 14.- Scanning electron fractographs of aluminum alloy 6061-T651 plate tensile specimens. (1 µm = 3.94×10^{-5} in.)

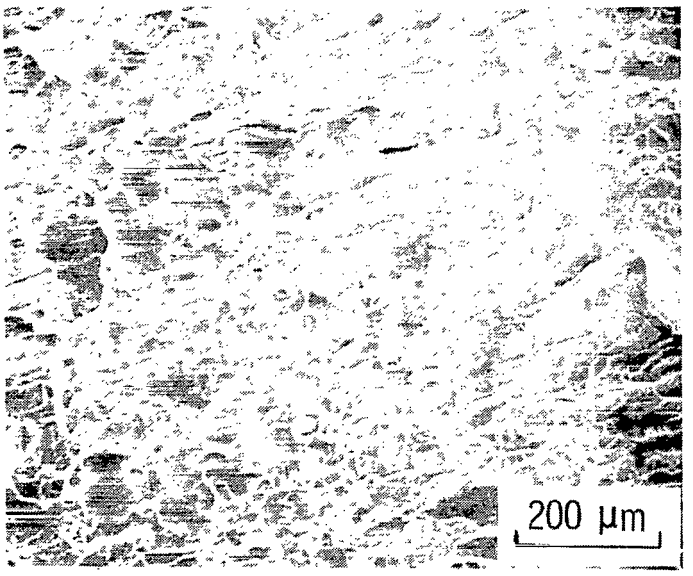

(a)

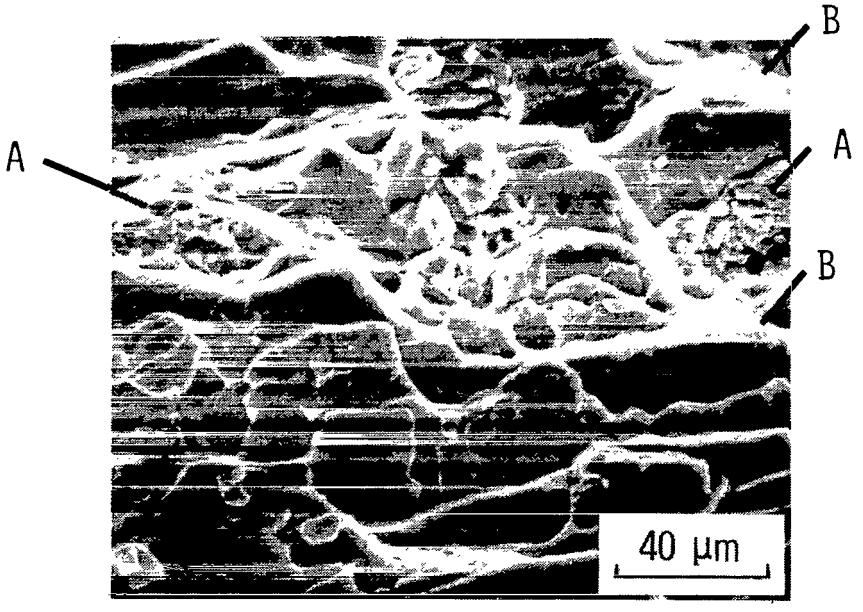

(b)

L-77-352

Figure 15.- Scanning electron fractographs of aluminum alloy 7075-T651 longitudinal plate tensile specimen. Areas labeled A identify dimples containing cracked particles; areas labeled B identify ductile tear. (1 µm = 3.94×10^{-5} in.)

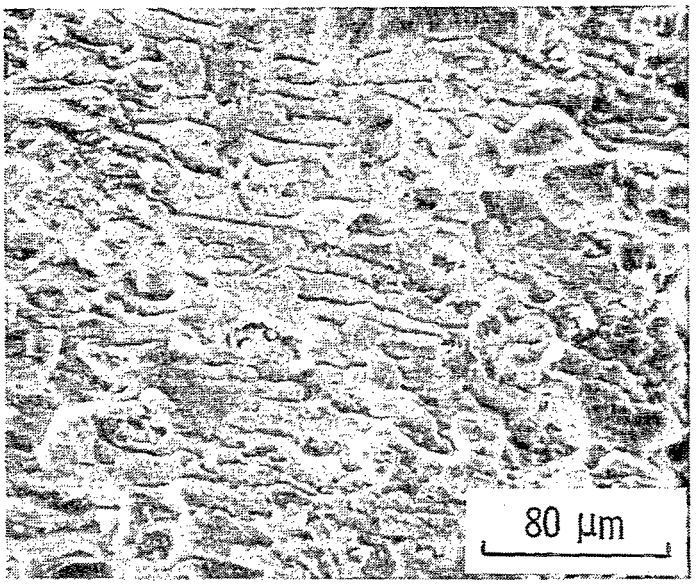

L-77-353

Figure 16.- Scanning electron fractograph of aluminum alloy 7178-T651 longitudinal plate tensile specimen.

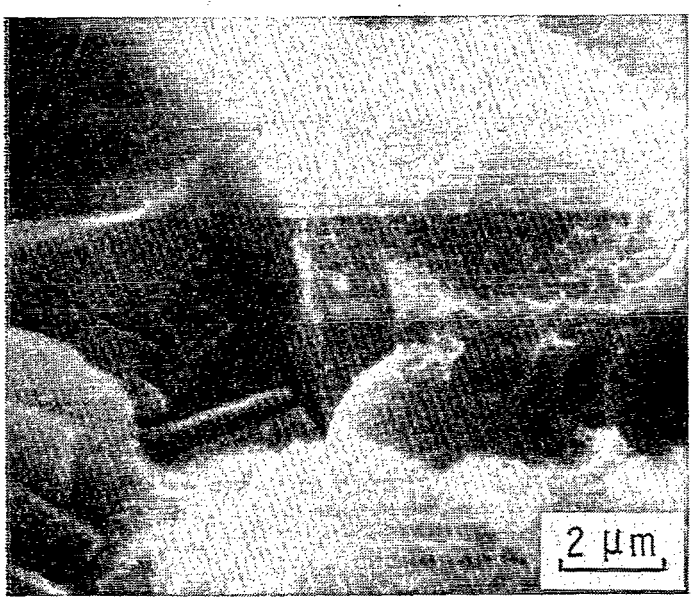

L-77-354

Figure 17.- High magnification scanning electron fractograph of aluminum alloy 7178-T651 longitudinal plate tensile specimen. (1 µm = 3.94×10^{-5} in.)

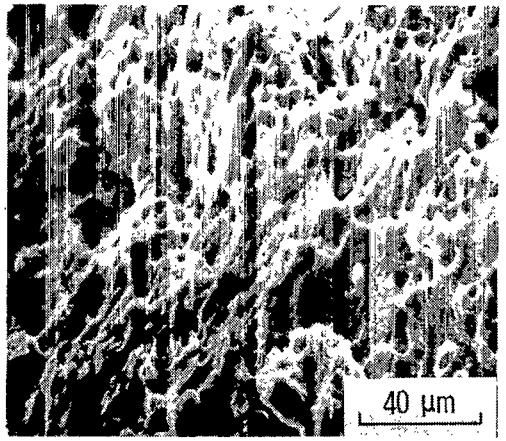

(a) 2024-T3.

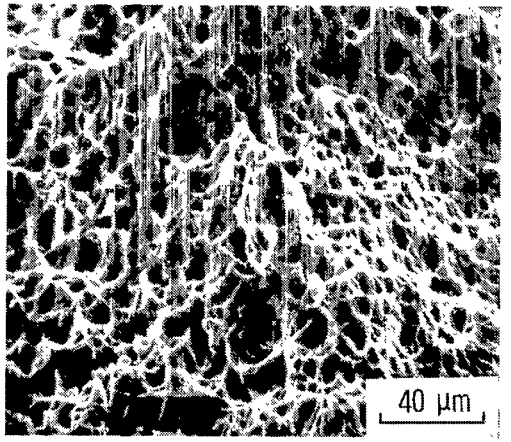

(b) 6061-T4.

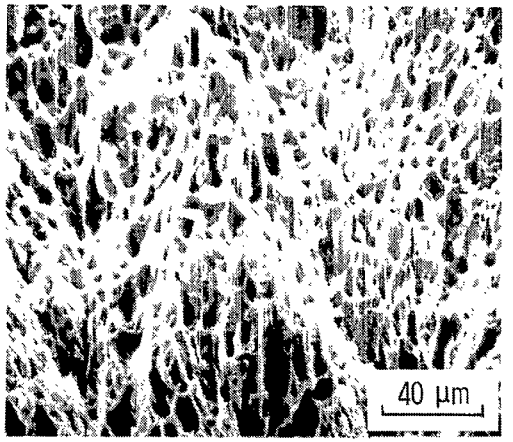

(c) 6061-T6.

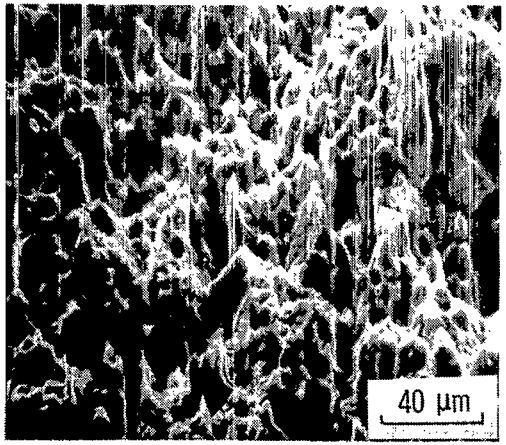

(d) 7075-T6.

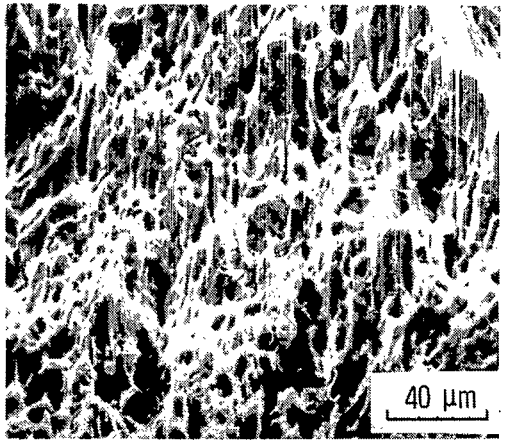

(e) 7178-T6.

L-77-355

Figure 18.- Scanning electron fractographs of longitudinal sheet tensile specimens of aluminum alloys investigated. (1 μm = 3.94×10^{-5} in.)

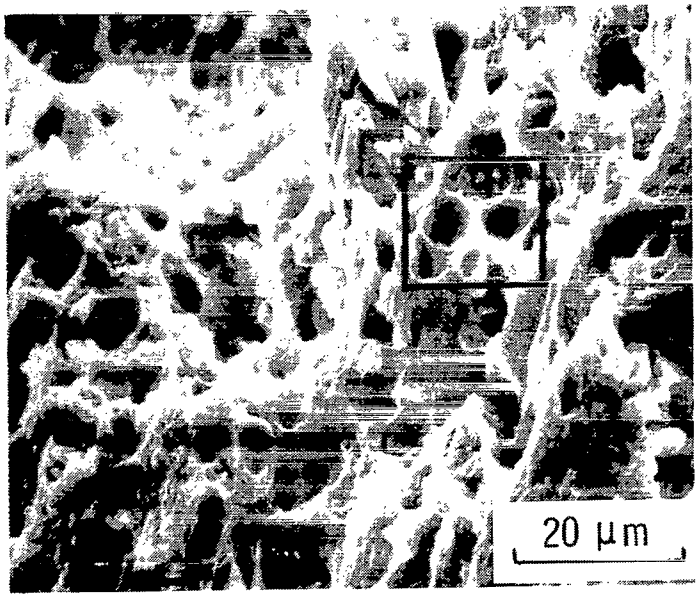

(a)

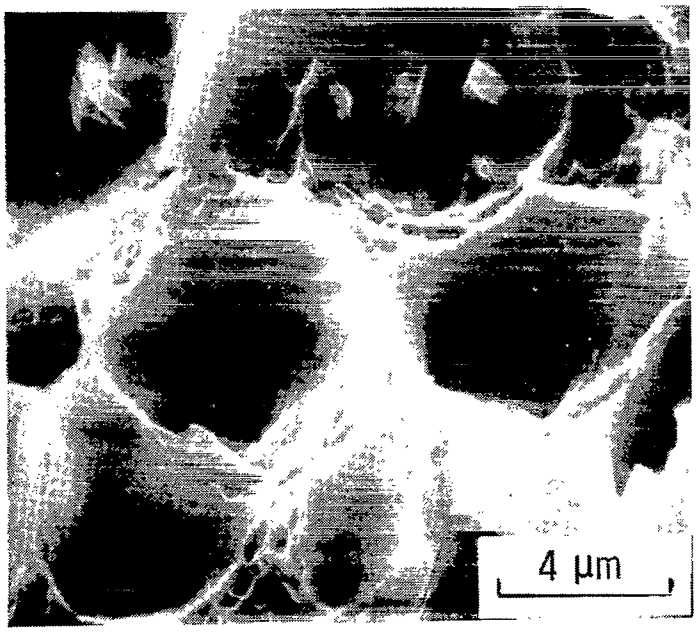

(b)

L-77-356

Figure 19.- Scanning electron fractographs of aluminum alloy 2024-T3 longitudinal sheet tensile specimen. Fractograph in (b) was obtained by magnifying area marked in (a). (1 µm = 3.94×10^{-5} in.)

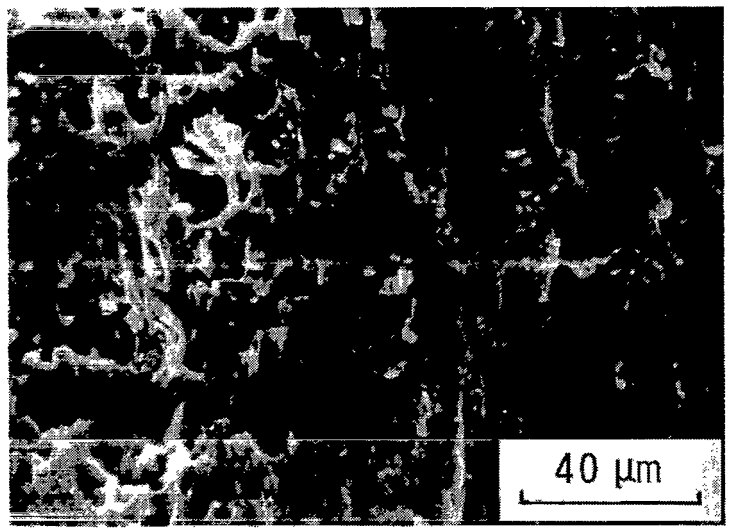

L-77-357

Figure 20.- Scanning electron fractograph of aluminum alloy 2024-T3 longitudinal sheet tensile specimen showing region that failed in shear. (1 µm = 3.94×10^{-5} in.)

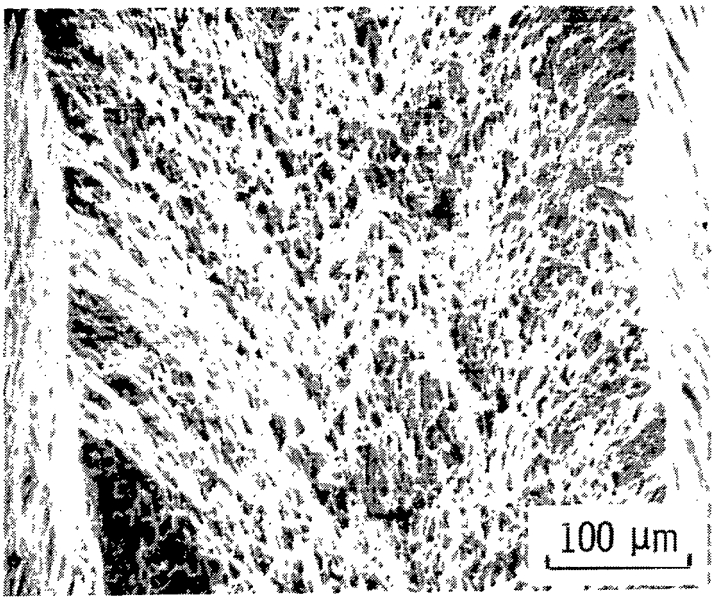

(a) 6061-T4.

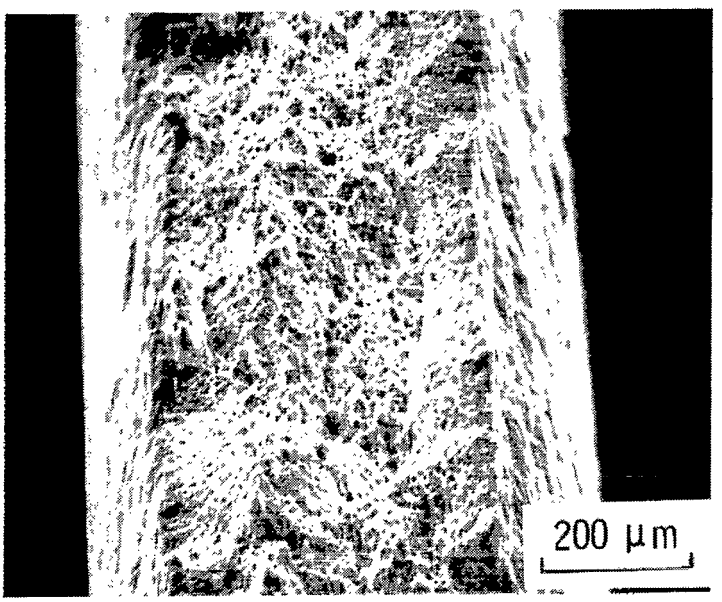

(b) 6061-T6.

L-77-358

Figure 21.- Scanning electron fractographs of two longitudinal sheet tensile specimens of aluminum alloy 6061. (1 µm = 3.94×10^{-5} in.)

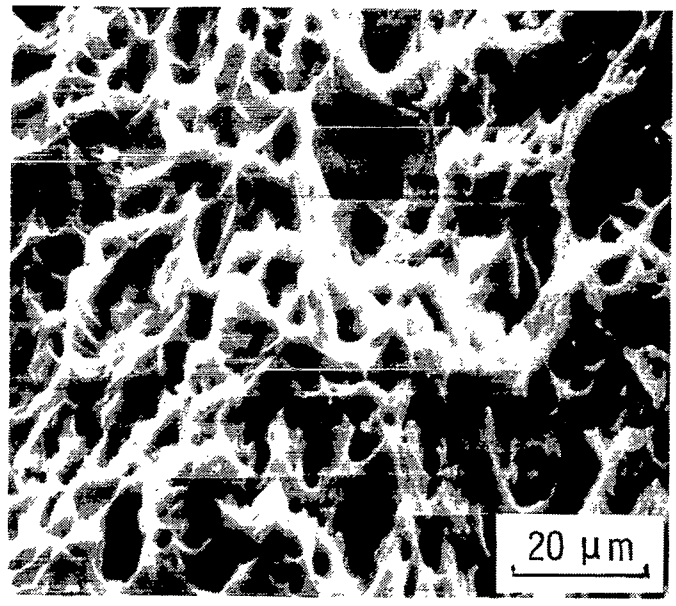

(a) 6061-T4.

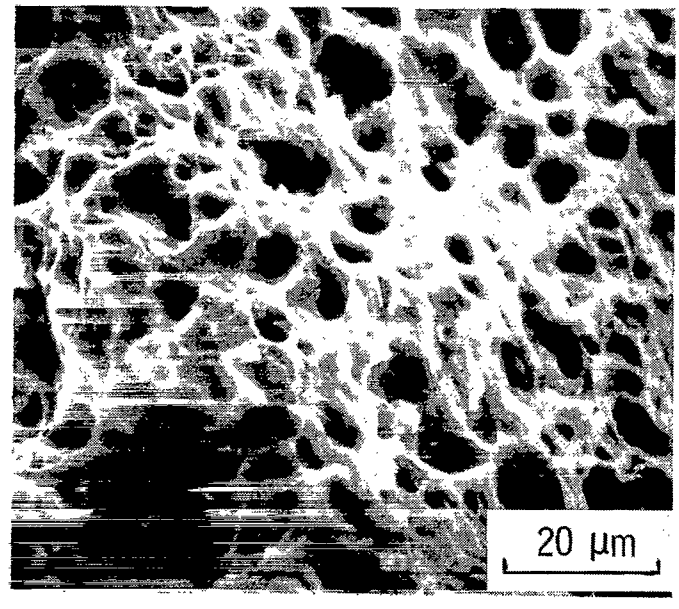

(b) 6061-T6.

L-77-359

Figure 22.- Scanning electron fractographs of two longitudinal sheet tensile specimens of aluminum alloy 6061. (1 µm = 3.94×10^{-5} in.)

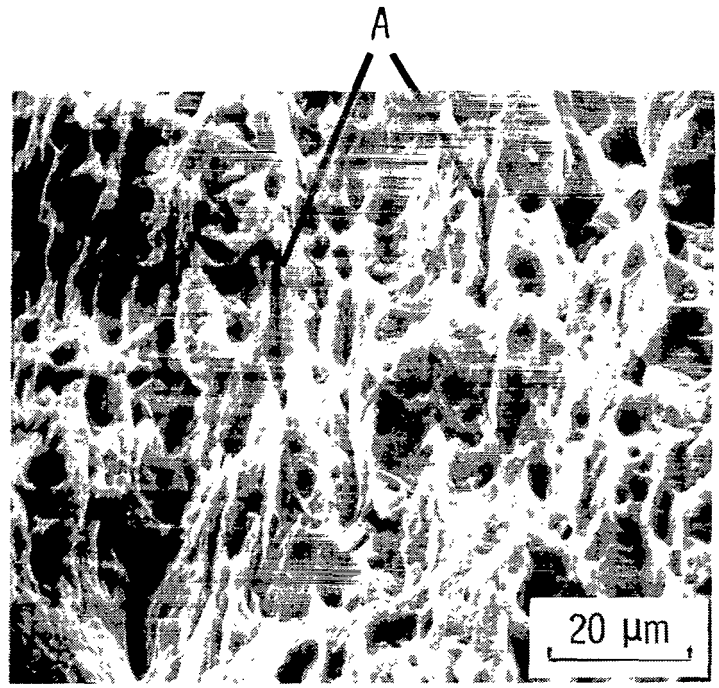

(a) 7075-T6 transverse specimen.

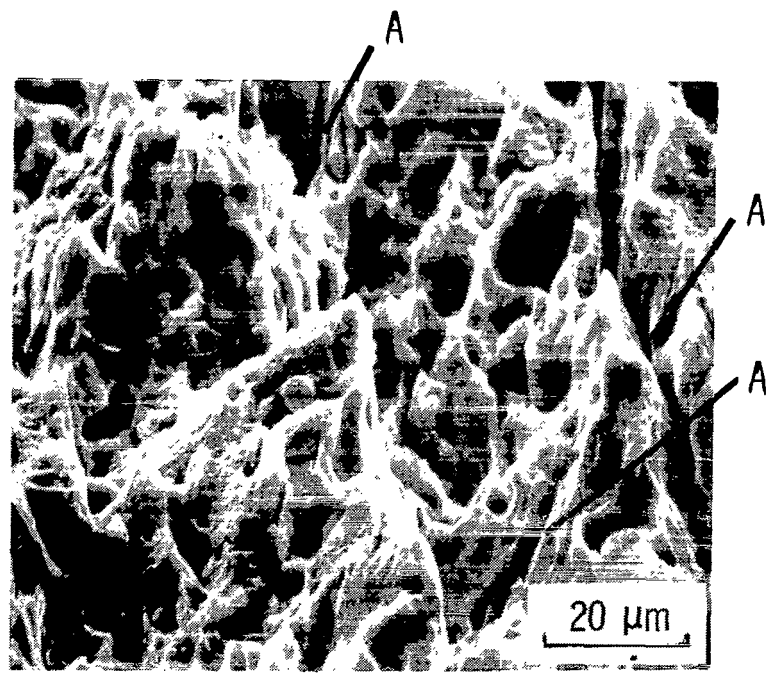

(b) 7178-T6 longitudinal specimen.

L-77-360

Figure 23.- Scanning electron fractograph of two sheet tensile specimens of 7000 series aluminum alloys. Areas labeled A identify grooves and secondary cracks. (1 μm = 3.94×10^{-5} in.)

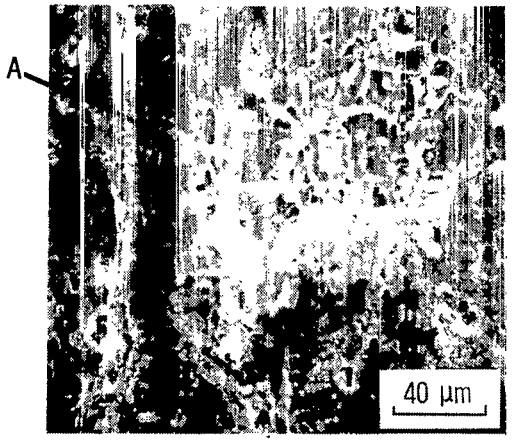

(a) 2024-T3 longitudinal specimen.

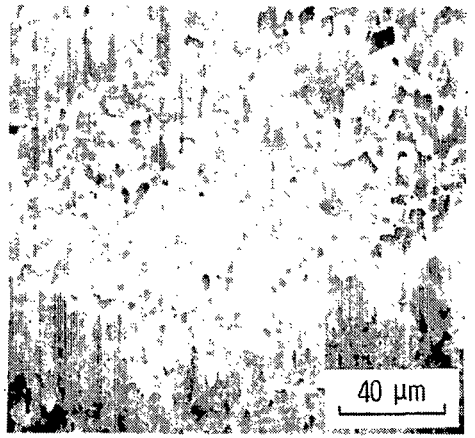

(b) 6061-T4 longitudinal specimen.

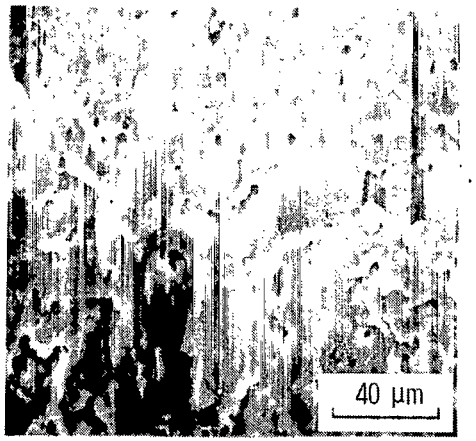

(c) 6061-T6 transverse specimen.

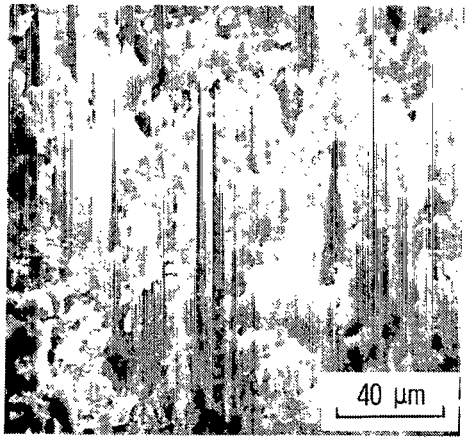

(d) 7075-T6 longitudinal specimen.

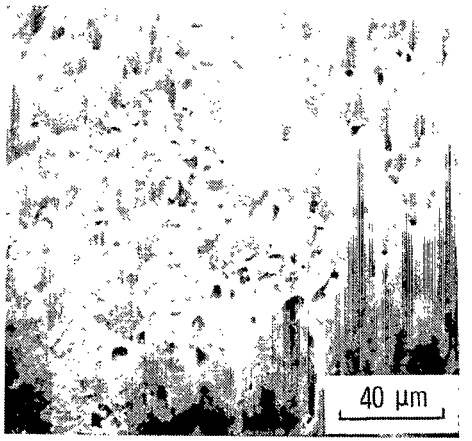

(e) 7178-T6 longitudinal specimen.

L-77-361

Figure 24.- Scanning electron fractographs of sheet shear specimens of aluminum alloys investigated, tested at cross-head separation rate of 2.54 mm/min (0.1 in./min). Area labeled A is shown at higher magnification in figure 25. (1 μm = 3.94×10^{-5} in.)

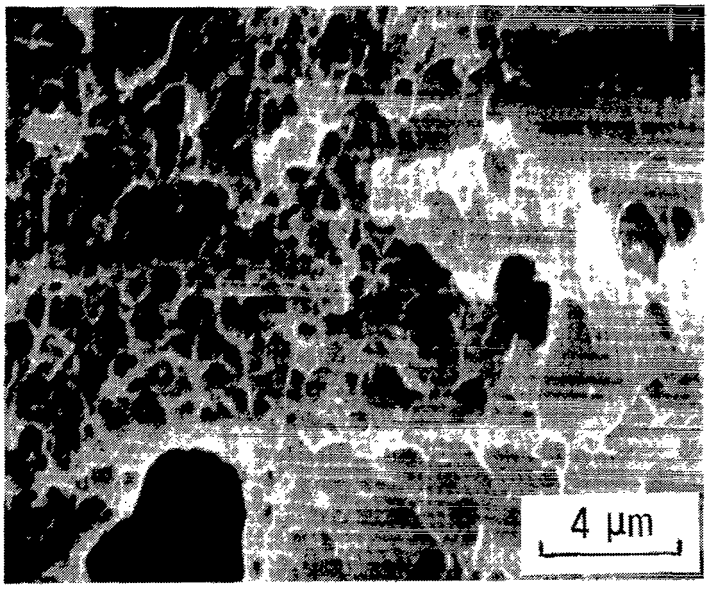

L-77-362

Figure 25.- Scanning electron fractograph of aluminum alloy 2024-T3 longitudinal sheet shear specimen tested at cross-head separation rate of 2.54 mm/min (0.1 in./min). (1 µm = 3.94×10^{-5} in.)

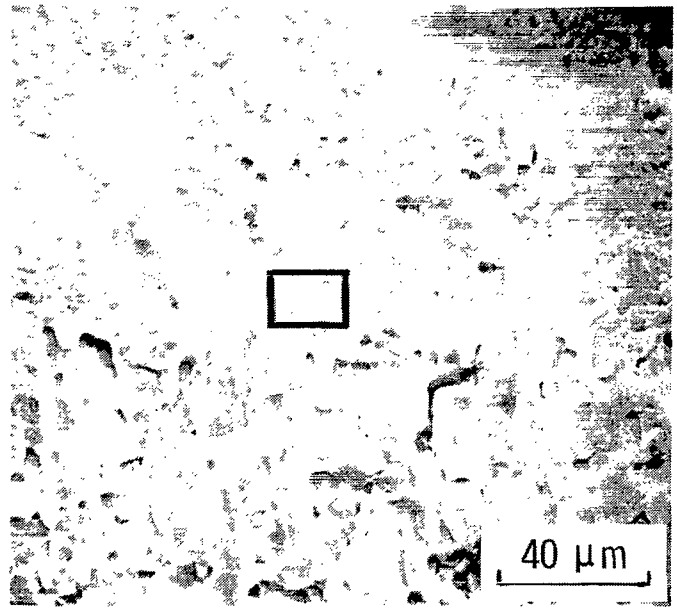

(a)

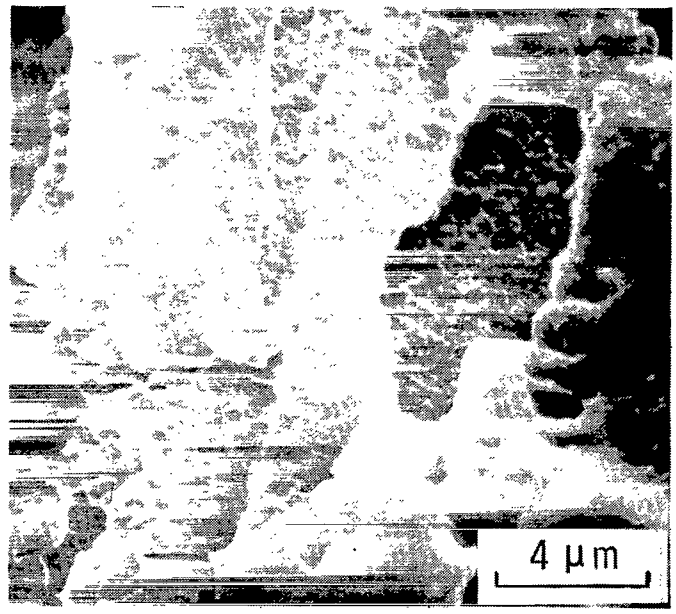

(b)

L-77-363

Figure 26.- Scanning electron fractographs of aluminum alloy 7178-T6 transverse sheet shear specimen tested at cross-head separation rate of 2.54 mm/min (0.1 in./min). Fractograph in (b) was obtained by magnifying area marked in (a). (1 µm = 3.94×10^{-5} in.)

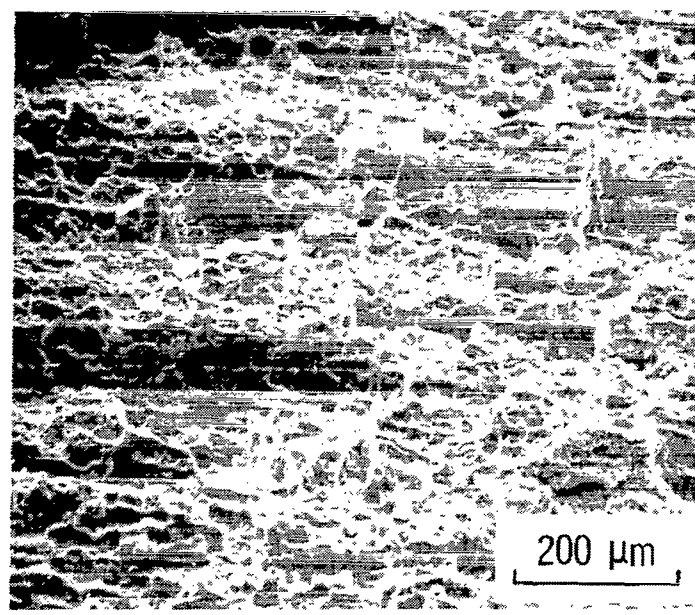

L-77-364

(a) Transverse specimen orientation.

Figure 27.- Scanning electron fractographs of precracked aluminum alloy 2024-T351 notch-bend specimens. (1 µm = 3.94×10^{-5} in.)

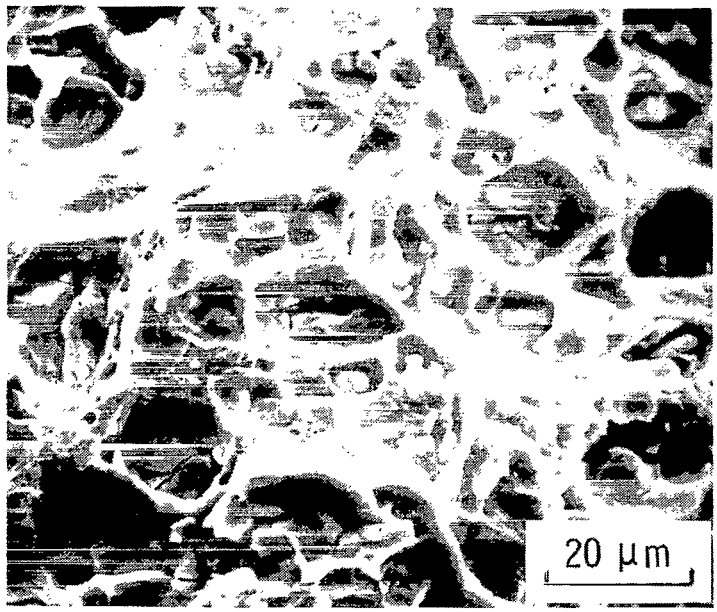

(b) Longitudinal specimen orientation.

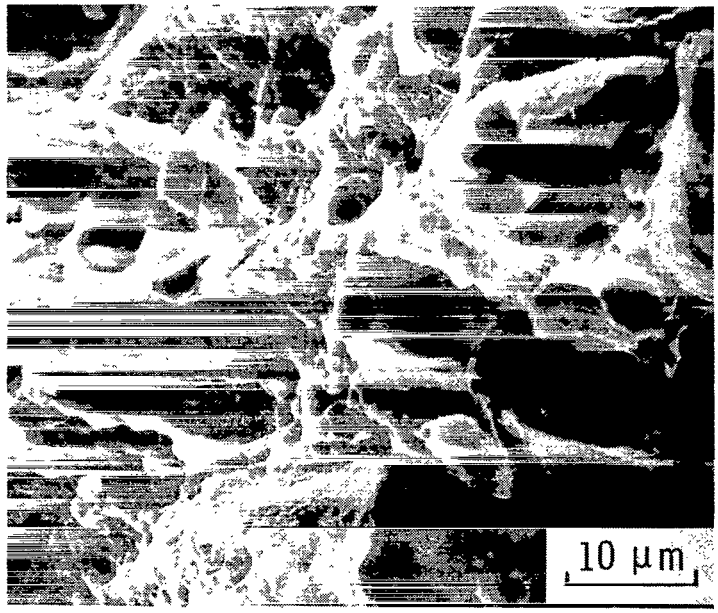

(c) Longitudinal specimen orientation.

L-77-365

Figure 27.- Concluded.

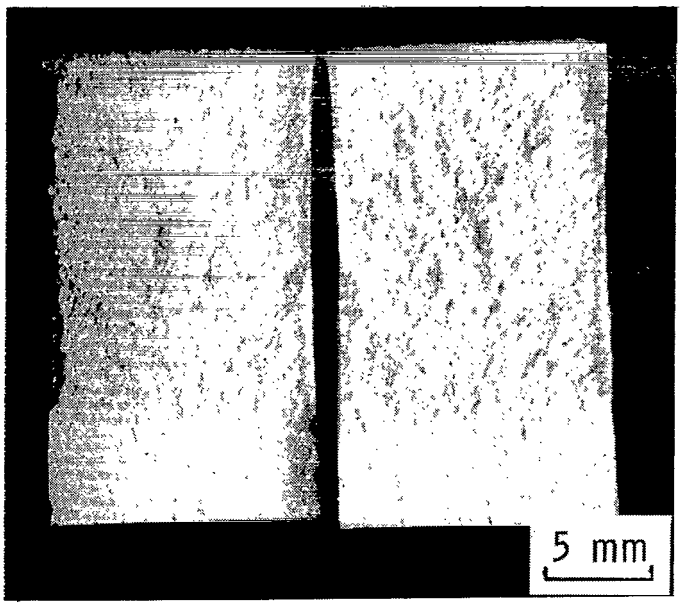

(a) Longitudinal specimen orientation.

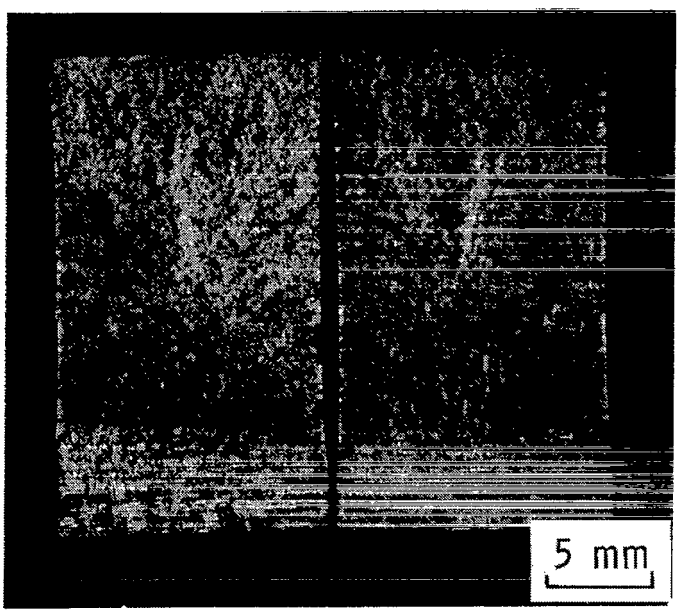

(b) Transverse specimen orientation.

L-77-366

Figure 28.- Optical macrographs of fracture surfaces of aluminum alloy 2024-T351 precracked notch-bend specimens. (1 mm = 3.94×10^{-2} in.)

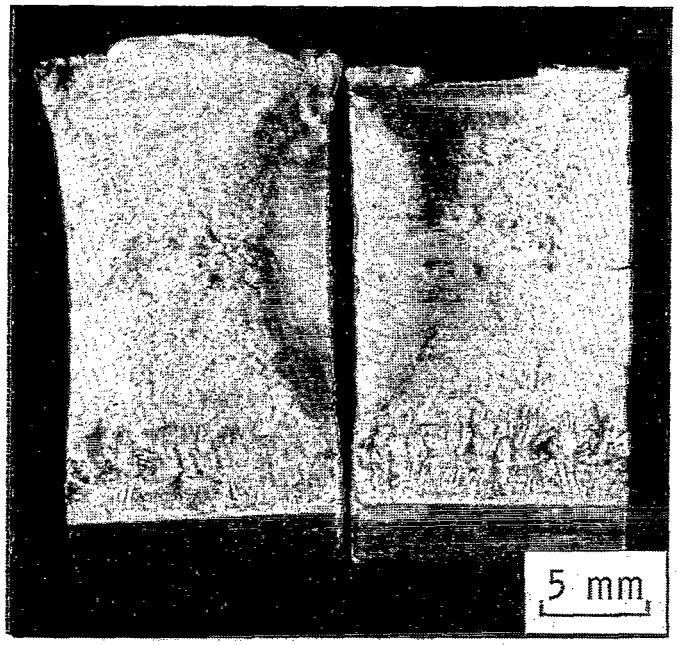

(a) 6061-T4 longitudinal specimen orientation.

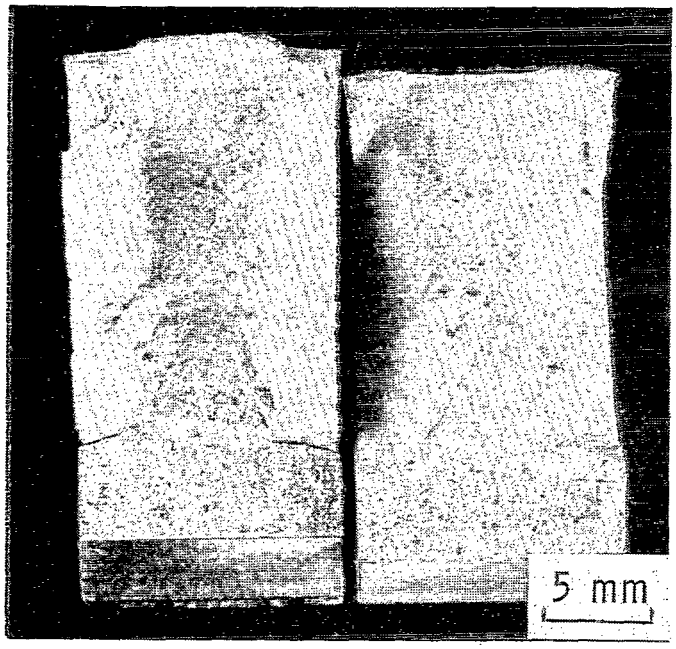

(b) 6061-T651 longitudinal specimen orientation.

L-77-367

Figure 29.- Optical macrographs of fracture surfaces of two 6000 series aluminum alloy precracked notch-bend specimens. (1 mm = 3.94×10^{-2} in.)

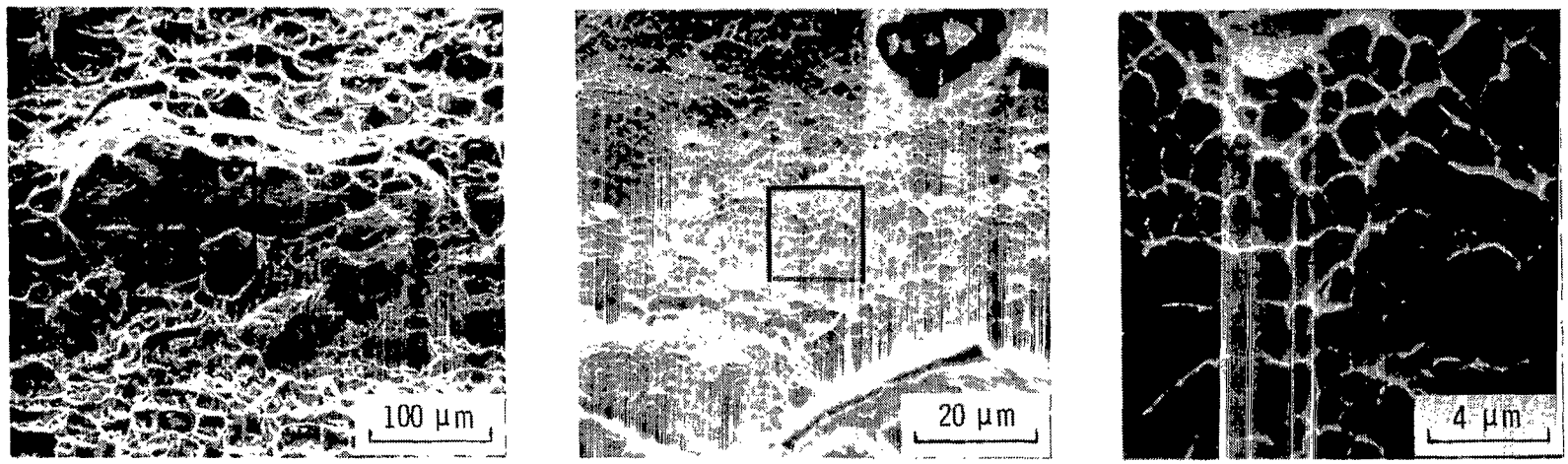

(a) (b) (c)

L-77-368

Figure 30.- Scanning electron fractographs of precracked aluminum alloy 6061-T651 notch-bend specimen tested in transverse specimen orientation. Fractographs in (b) and (c) were obtained by magnifying areas marked in (a) and (b), respectively. (1 µm = 3.94×10^{-5} in.)

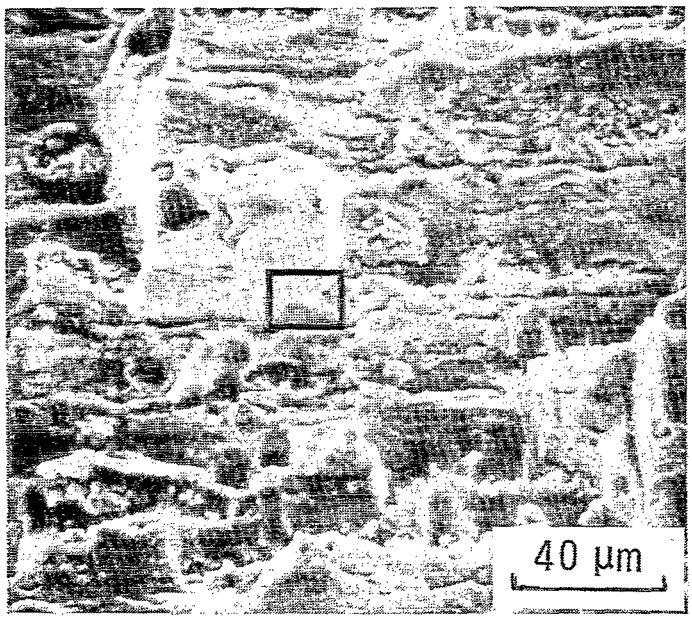

(a)

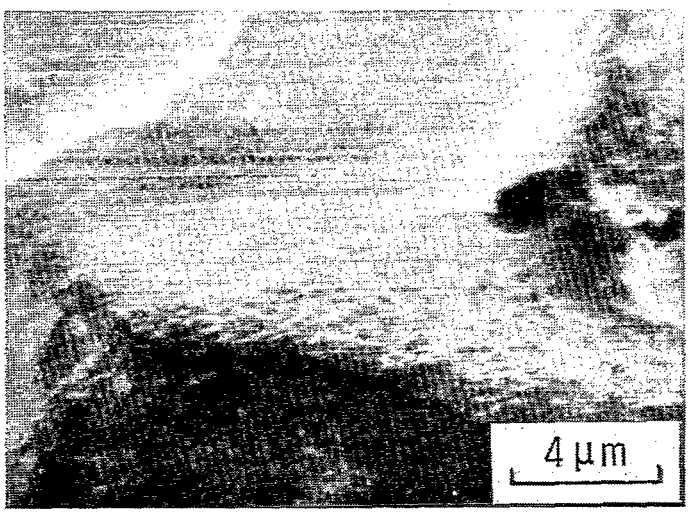

(b)

L-77-369

Figure 31.- Scanning electron fractographs of aluminum alloy 7075-T651 precracked notch-bend specimen tested in transverse orientation. Fractograph in (b) was obtained by magnifying area marked in (a). (1 µm = 3.94×10^{-5} in.)

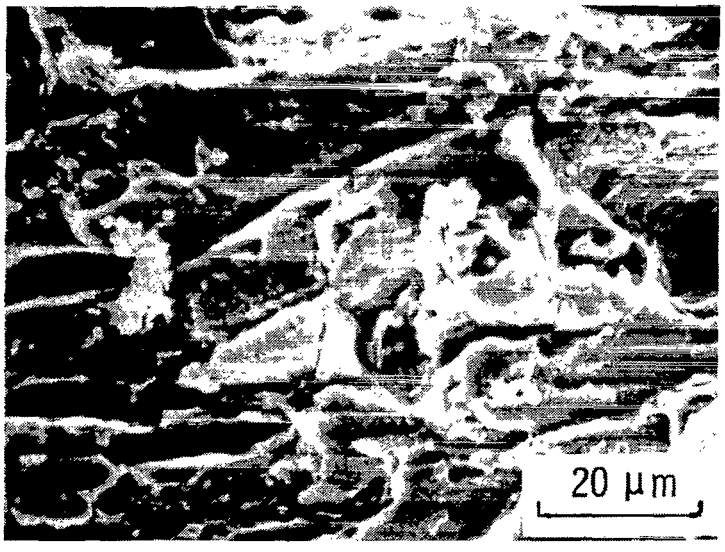

(a)

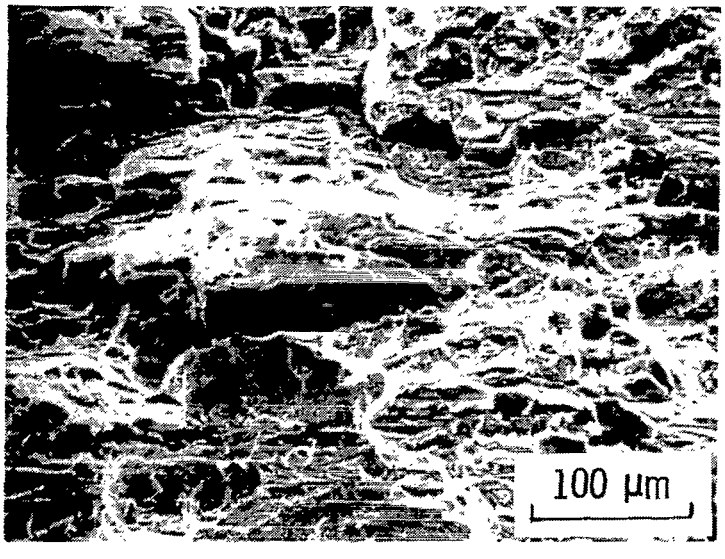

(b)

L-77-370

Figure 32.- Scanning electron fractographs showing deep grooves and secondary cracking in aluminum alloy 7075-T651 precracked notch-bend specimen tested in longitudinal orientation. (1 µm = 3.94×10^{-5} in.)

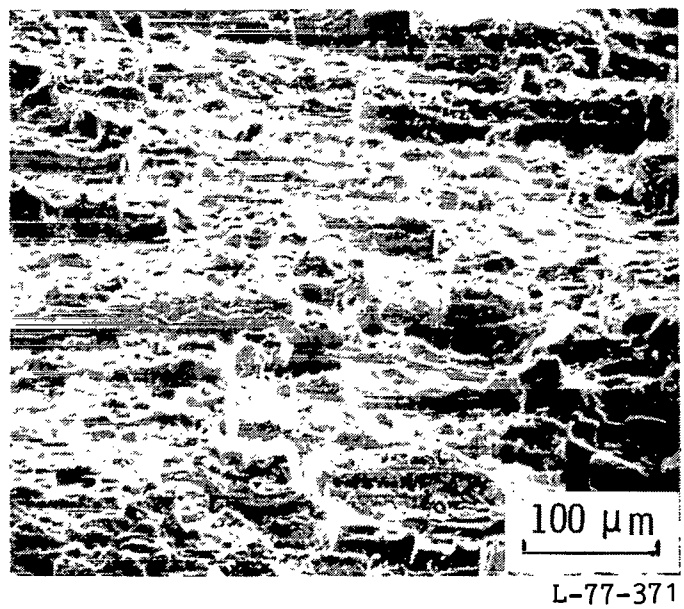

(a)

Figure 33.- Scanning electron fractographs of aluminum alloy 7178-T651 precracked notch-bend specimen tested in transverse orientation. Areas A, B, and C in (d) and (e) identify large dimples, fine dimples, and ductile tearing, respectively. (1 μm = 3.94×10^{-5} in.)

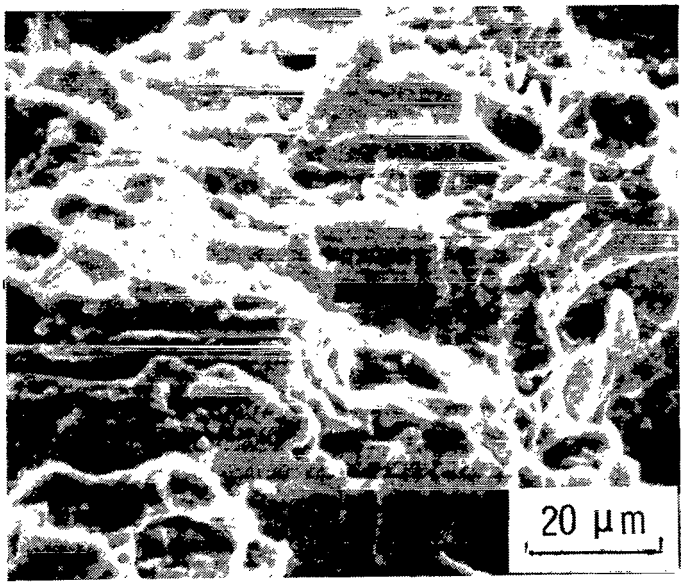

(b)

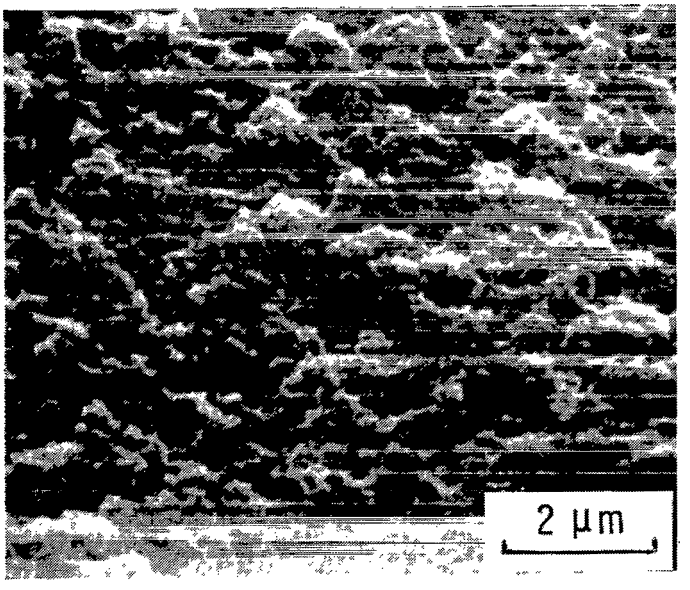

(c)

L-77-372

Figure 33.- Continued.

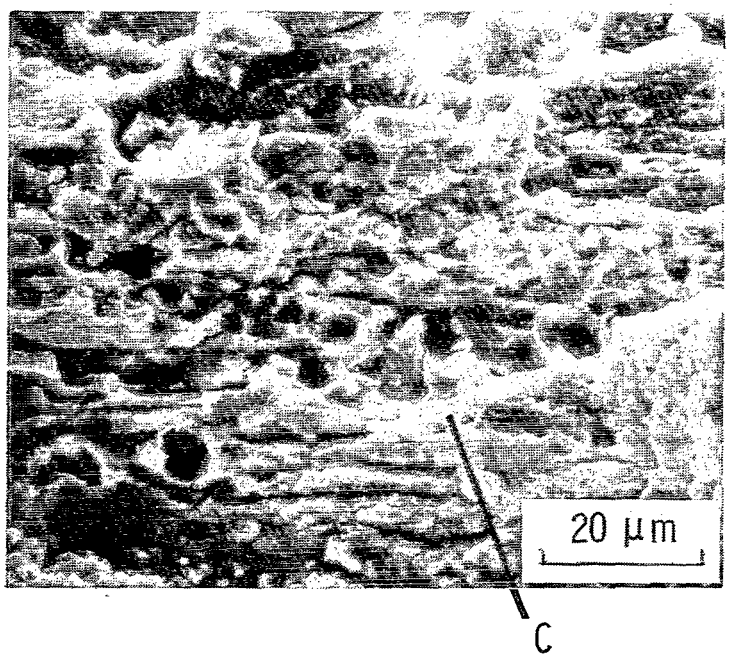

(d)

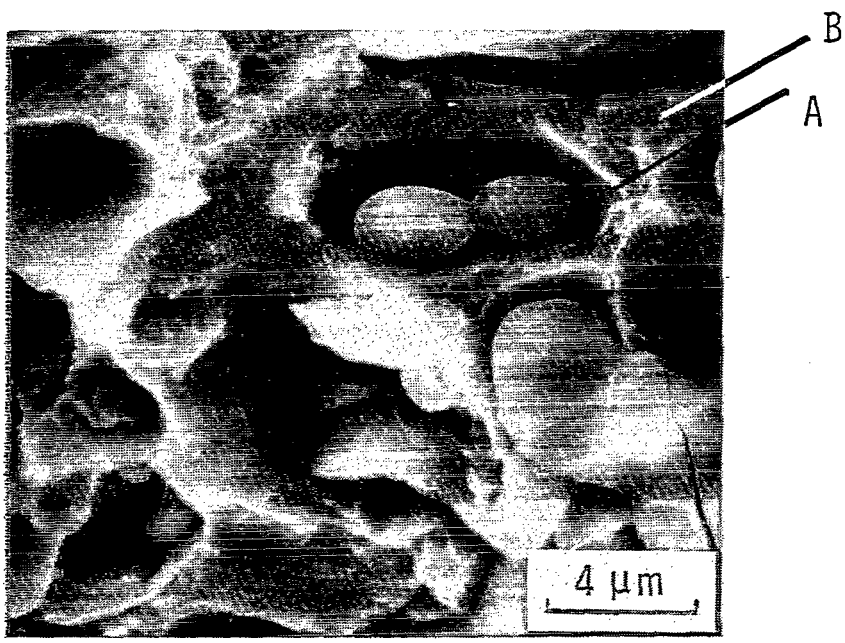

(e)

L-77-373

Figure 33.- Concluded.

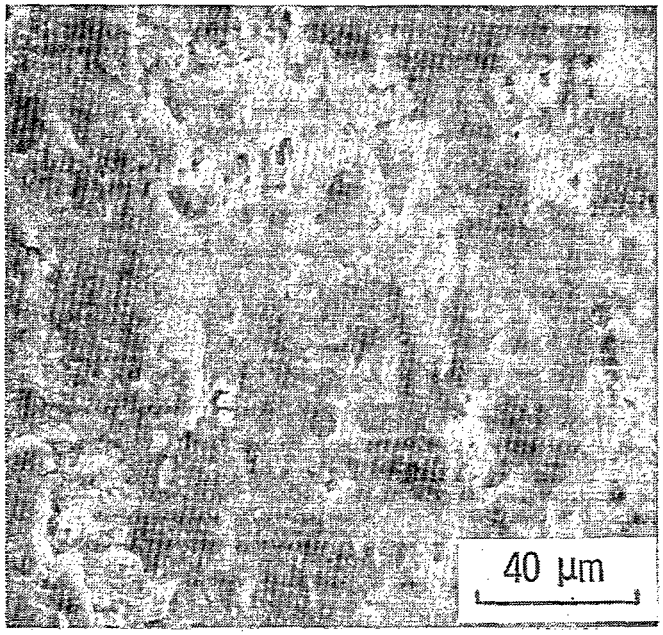

(a) Tested at cross-head separation rate of 2.54 mm/min (0.1 in./min).

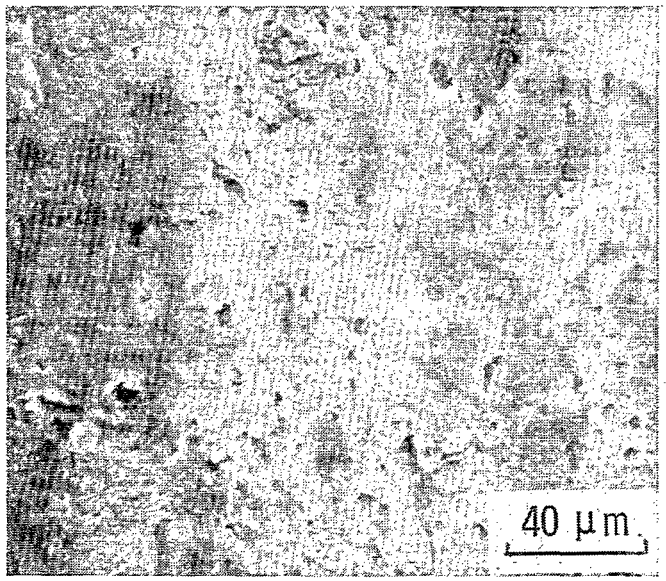

(b) Tested at cross-head separation rate of 76.2 mm/min (3 in./min).

L-77-374

Figure 34.- Scanning electron fractographs of aluminum alloy 7075-T6 longitudinal sheet shear specimens tested at different cross-head separation rates. (1 µm = 3.94×10^{-5} in.)

1. Report No.	2. Government Accession No.	3. Recipient's Catalog No.
NASA TP-1086		

4. Title and Subtitle	5. Report Date
METALLURGICAL CHARACTERIZATION OF THE FRACTURE OF SEVERAL HIGH STRENGTH ALUMINUM ALLOYS	December 1977
	6. Performing Organization Code
7. Author(s)	8. Performing Organization Report No.
M. Dilip Bhandarkar and W. Barry Lisagor	L-11255
	10. Work Unit No.
9. Performing Organization Name and Address	505-01-34-03
NASA Langley Research Center Hampton, VA 23665	11. Contract or Grant No.
	13. Type of Report and Period Covered
12. Sponsoring Agency Name and Address	Technical Paper
National Aeronautics and Space Administration Washington, DC 20546	14. Sponsoring Agency Code

15. Supplementary Notes

M. Dilip Bhandarkar: National Research Postdoctoral fellow, now with ANAMET Laboratories, Inc., Berkeley, California.

W. Barry Lisagor: Langley Research Center, Hampton, Virginia.

16. Abstract

The fracture behavior for structural aluminum alloys (2024, 6061, 7075, and 7178) has been examined in selected heat treatments. The investigation included tensile, shear, and precracked notch-bend specimens fractured at ambient temperature under monotonic loading. Specimens were obtained from thin sheets and thick plates and were tested in longitudinal and transverse orientations at different strain rates. Microstructures of alloys were examined using the optical microscope and the scanning electron microscope with associated energy dispersive X-ray chemical analysis. Several different types of second-phase particles, some not reported by other investigators, were identified in the alloys. Fracture morphology was related to microstructural variables, test variables, and type of commercial product. Specimen orientation examined in the present investigation had little effect on fracture morphology. Test strain rate changes resulted in some change in shear fracture morphology, but not in fracture morphology of tensile specimens.

17. Key Words (Suggested by Author(s))		18. Distribution Statement
Fracture (materials)	Microstructure	Unclassified - Unlimited
Tensile	Aluminum alloys	
Shear		
Notch bend		
Fractography		Subject Category 25

19. Security Classif. (of this report)	20. Security Classif. (of this page)	21. No. of Pages	22. Price*
Unclassified	Unclassified	68	$5.25

* For sale by the National Technical Information Service, Springfield, Virginia 22161

NASA-Langley, 1977

National Aeronautics and
Space Administration

Washington, D.C.
20546

Official Business
Penalty for Private Use, $300

THIRD-CLASS BULK RATE

Postage and Fees Paid
National Aeronautics and
Space Administration
NASA-451

442 C01 C1 U C 770610 S00903DS
DEPT OF THE AIR FORCE
AF WEAPONS LABORATORY
ATTN: TECHNICAL LIBRARY (SUL)
KIRTLAND AFB NM 87117

NASA

If Undeliverable (Section 158
Postal Manual) Do Not Return